

Supercritical Fluid Deposition for Semiconducting Polymer

**by
Simran**

Integrated Masters (Chemistry), Birla Institute of Technology India, 2018

Thesis Submitted in Partial Fulfillment of the
Requirements for the Degree of
Master of Science

in the
Department of Chemistry
Faculty of Science

© Simran 2022

SIMON FRASER UNIVERSITY

Fall 2022

Copyright in this work is held by the author. Please ensure that any reproduction or re-use is done in accordance with the relevant national copyright legislation.

Declaration of Committee

Name: Simran

Degree: Master of Science (Chemistry)

Title: Supercritical Fluid Deposition for
Semiconducting Polymer

Committee: **Chair: Paul Li**
Professor, Chemistry

Loren Kaake
Supervisor
Associate Professor, Chemistry

Byron Gates
Committee Member
Professor, Chemistry

Vance Williams
Committee Member
Professor, Chemistry

Gary Leach
Examiner
Associate Professor, Chemistry

Abstract

The physical supercritical fluid deposition is a method of thin film deposition that allows high molecular weight materials to be deposited onto curved and flexible substrates to form patterns with high spatial resolution. The preferred mode of deposition relies on a maximum in the isobaric solubility to precipitate material onto a heated substrate. This typically occurs at pressures exceeding the critical pressure of the solvent, hence the technique is termed supercritical fluid deposition. Because the technique relies on the solubility properties of the solvent-solute system, one of the most important factors in determining the optimized deposition conditions is solvent selection. Here, we demonstrate that for poly(3-hexyl thiophene) (P3HT), there are three qualitatively different types of solvents, only one of which is appropriate for physical supercritical fluid deposition on heated substrates. Over-powered solvents are ineffective for the physical supercritical fluid deposition because they lack a maximum in the isobaric solubility. Underpowered solvents are unable to dissolve the deposition material. Optimum solvents dissolve the material effectively and exhibit a maximum isobaric solubility over the working temperature range of the deposition chamber. In addition, we demonstrate the effect of adding an overpowered solvent to an underpowered solvent and an optimum solvent. Only the mixture with an optimum solvent shows the necessary characteristics for physical supercritical fluid deposition. In sum, the work demonstrates clear guidelines for solvent selection that will allow for the deposition of a wider range of materials. Furthermore, the films are deposited to achieve better uniformity and smoothness.

Keywords: Supercritical fluid; Thin film deposition; Poly(3-hexyl thiophene); Ultraviolet-visible spectroscopy; Isobaric solubility

This thesis is dedicated to my constants.

Acknowledgements

I deeply express my gratitude to my supervisor Dr. Loren Kaake, Associate Professor in the Department of Chemistry at Simon Fraser University, Burnaby. I was fortunate enough to receive guidance from him as a mentor who supported me immensely throughout my research. I have greatly benefitted from his wise counsel associated with experiments and presenting my work. I would always remain indebted to him for empowering me to learn.

I would like to express my gratitude to my committee members- Dr. Byron Gates and Dr. Vance Williams for their support and guidance. I thank them for the illuminating discussions and suggestions that helped me throughout my research. Also, I would like to thank Dr. Byron Gates for permitting us to use their optical microscope.

I would like to extend my heartfelt gratitude to the staff of the Department of Chemistry, Science Technical Services, and 4D labs. I would also like to thank all of them for always helping me.

I would like to thank my friends for their constant help and encouragement. I will cherish the moments spent with all of them.

Finally, I express my forever indebtedness to my family. I am grateful for their unconditional love and support for me. I thank them all for being my pillars of strength. Words fail to describe their contributions to my life.

Table of Contents

Declaration of Committee	ii
Abstract	iii
Dedication	iv
Acknowledgements	v
Table of Contents	vi
List of Tables	viii
List of Figures	ix
List of Acronyms and Symbols	xi
Chapter 1. Introduction	1
1.1. Thesis Outline	1
1.2. Structure	3
1.2.1. Background	3
1.2.2. Organic Semiconductors	5
1.3. Doping in Organic Semiconductors	7
1.4. Types of Organic Semiconductors	8
1.5. Charge Transport Mechanisms	10
1.5.1. Band Structure	11
1.5.2. Disordered-based Mechanism	12
1.6. Impact of Structure on Charge Transport	13
1.6.1. Regioregularity	13
1.6.2. Molecular Weight	13
1.7. Supercritical fluid	15
1.7.1. Gibbs Free Energy	18
1.7.2. Flory Huggins Theory	19
1.8. Fluid Flow	19
1.8.1. Rayleigh Number	20
1.9. Ultraviolet-visible Spectroscopy	21
1.9.1. Franck Condon Principle	21
1.9.2. Beer-Lambert Law	22
1.10. Organic Field Effect Transistors	23
Chapter 2. Methods	27
2.1. Supercritical Fluid Chamber	27
2.2. Experimental Procedures	30
2.2.1. Substrate Cleaning	34
2.2.2. Sample Preparation	35
2.3. Ultraviolet-visible Spectroscopy	35
2.4. Film Deposition	36
2.5. PID controller	37
2.6. Optical Microscope	39
2.7. Probe Station	40

Chapter 3. Results	42
3.1. Introduction.....	42
3.2. Experimental	45
3.3. Results and discussion.....	47
3.3.1. Solubility study of P3HT in pentane.....	47
3.3.2. Solubility study of P3HT in solutions containing novoc	49
3.3.3. Solubility study of P3HT in solutions containing solstice.....	51
3.3.4. Film growth of P3HT using p-SFD deposition technique.....	55
3.4. Summary.....	55
Chapter 4. Conclusions and Future Directions	57
References	61

List of Tables

Table 2.1.	Metals used to build thermocouples for different temperature ranges.....	33
Table 4.1.	Summary of behavior of P3HT in different solvent systems in p-SFD.....	58

List of Figures

Figure 1.1.	Deposition techniques (a) Inkjet Printing (b) Gravure Printing (c) Vacuum Deposition (d) Spin Coating	2
Figure 1.2.	Shapes of s,p, and d atomic orbitals.....	4
Figure 1.3.	Formation of Bonding and Antibonding molecular orbitals by the interaction of atomic orbitals.....	5
Figure 1.4.	Delocalization of π electrons in Benzene.....	6
Figure 1.5.	Energy-level splitting in alkenes with increasing conjugation length	7
Figure 1.6.	p-type and n-type doping in organic semiconductor	8
Figure 1.7.	Structures of small molecules.....	9
Figure 1.8.	Structures of organic semiconducting polymers	10
Figure 1.9.	Band gap in conductor, semiconductor, and insulator	12
Figure 1.10	Hopping transport between localized state	12
Figure 1.11.	HH, HT, TT in P3HT	14
Figure 1.12.	Regioregular (left) and regiorandom (right) P3HT.....	15
Figure 1.13.	Phase diagram showing the supercritical fluid region	16
Figure 1.14.	Phase transition in supercritical fluid (A) two distinct phases (liquid and gas) (B) the phases start to diminish (C) liquid and gas phases become more similar (D) liquid and gas phases become indistinguishable.....	17
Figure 1.15.	Isotherms showing van der Waals equation of state.....	18
Figure 1.16.	Lattice model of a polymer solution	19
Figure 1.17.	Schematic of Laminar and Turbulent fluid flow	20
Figure 1.18.	Schematic absorption spectra (top) and potential curve diagram (bottom)	22
Figure 1.19.	Configurations of organic field-effect transistors a. bottom gate bottom contact b. bottom gate top contact c. top gate bottom contact d. top gate top contact	24
Figure 1.20.	Operating regimes a) linear regime b) start of saturation regime at pinch-off c) saturation regime and corresponding current-voltage characteristics	25
Figure 2.1.	Drawing of the supercritical fluid chamber	28
Figure 2.2.	Overview of gas manifold	29
Figure 2.3.	Overview of pipes and valves of the SCF chamber	30
Figure 2.4.	Overview of regulator and valves connected in the SCF chamber.....	31
Figure 2.5.	Schematic of chamber connected to power supply and temperature control unit	31
Figure 2.6.	Schematic of pressure generator connected to the SCF chamber.....	34
Figure 2.7.	Schematic of UV-visible spectroscopy with SCF chamber setup	35
Figure 2.8.	Sample holder view from the side (left), top (center), and bottom (right).	37
Figure 2.9.	Block diagram of PID controller	38

Figure 2.10.	Proportional controller	38
Figure 2.11.	Integral controller	39
Figure 2.12.	Derivative controller	39
Figure 2.13.	Probe station.....	41
Figure 3.1.	Chemical structures of compounds used in this study:P3HT, Novec and Solstice	46
Figure 3.2.	Solubility data for P3HT in pentane. (a) UV-Vis of P3HT in n-pentane collected at 1500 psi (b) Absorbance at 490 nm for several pressures as a function of temperature (c) Absorbance at 490 nm for several temperatures as a function of pressure	48
Figure 3.3.	Solubility data for P3HT in novec. (a) UV-Vis of P3HT in several solutions containing novec collected at 1000 psi and 150 °C (b) Absorbance as a function of temperature at 1000 psi and 490 nm (c) Absorbance as a function of temperature at 1000 psi and 550 nm.....	50
Figure 3.4.	Solubility data for P3HT in novec and pentane. (a) UV-Vis of P3HT in novec and pentane collected at 500 psi (b) at 1000 psi (c) 1500 psi (d) at 2500 psi	51
Figure 3.5.	Solubility data for P3HT in solstice. (a) UV-Vis of P3HT in solstice collected at 1250 psi (b) Absorbance at 490 nm for several pressures (c) Absorbance at several temperatures as a function of pressure	52
Figure 3.6.	Solubility data of P3HT in solstice/toluene mixtures. (a) UV-Vis of P3HT in solstice/toluene (5%) collected at 750 psi (b) Absorbance for several pressures as a function of temperature (c) Absorbance at several temperatures as a function of pressure	54
Figure 3.7.	Optical microscope image taken at a resolution of 50 μm showing a thin film of P3HT deposited on a resistively heated ITO glass substrate from a solstice/toluene (5%) solution.....	55
Figure 4.1.	Output curve (left) and Transfer curve (right) for P3HT based organic field-effect transistor.....	59
Figure 4.2.	Optical images showing optimization of uniformity in P3HT films by p-SFD deposited on ITO coated glass (a) at 200 μm magnification (b) 20 μm magnification (c) at 50 μm magnification	60

List of Acronyms and Symbols

A	Absorbance
BeCu	Beryllium Copper
CCD	Charge-Coupled Device
<i>E</i>	Electric Field
ϵ	Molar Absorptivity
FET	Field-Effect Transistor
F8BT	Poly(9,9-dioctylfluorene-alt-benzothiadiazole)
G	Gibbs Free Energy
H	Enthalpy
HOMO	Highest Occupied Molecular Orbital
I	Intensity
ITO	Indium Tin Oxide
LUMO	Lowest Unoccupied Molecular Orbital
MEH-PPV	Poly[2-methoxy-5-(2-ethylhexyloxy)-1,4-phenylenevinylene]
M_n	Number Average Molecular Weight
M_w	Weight Average Molecular Weight
P3HT	Poly(3-hexylthiophene)
PBTTT	Poly[2,5-bis(3-tetradecylthiophen-2-yl)thieno[3,2-b]thiophene]
P_c	Critical Pressure
PC60BM	[6,6]-phenyl-C61-butyric acid methyl ester
PC70BM	[6,6]-phenyl-C71-butyric acid methyl ester
PCDTBT	Poly[N-9'-heptadecanyl-2,7-carbazole-alt-5,5-(4',7'-di-2-thienyl-2',1',3'-benzothiadiazole)]
PCPDTBT	Poly[2,6-(4,4-bis(2-ethylhexyl)-4H-cyclopenta[2,1-b;3,4-b]dithiophene)-alt-4,7-(2,1,3-benzothiadiazole)]
PDPP-TTT	Poly[2,5-(2-octyldodecyl)-3,6-diketopyrrolopyrrole-alt-5,5-(2,5-di(thien-2-yl)thieno [3,2-b]thiophene)]

p-SFD	Physical Supercritical Fluid Deposition
PTB7	Poly [[4,8-bis[(2-ethylhexyl)oxy]benzo[1,2-b:4,5-b']dithiophene-2,6-diyl][3-fluoro-2-[(2-ethylhexyl)carbonyl]thieno[3,4-b]thiophenediyl]]
Ra	Rayleigh Number
RFID	Radio Frequency Identification
RR	Regioregular
RRa	Regiorandom
S	Entropy
SCF	Supercritical Fluid
SubPc	Boron subphthalocyanine chloride
T _c	Critical Temperature
UV-vis	Ultraviolet-visible
M	Charge carrier mobility
λ	Wavelength

Chapter 1. Introduction

The scientific investigations in the field of organic electronics have increased tremendously over the last few decades. A groundbreaking discovery reported in 1977 reported the metallic conductivity in polyacetylene.¹ This revolutionary discovery led to Nobel Prize in Chemistry for Shirakawa, MacDiarmid, and Heeger in 2000. Organic semiconductors have emerged as a category of materials that have promising potential to replace conventional semiconductors in electronic devices.² The advancement in the research has engendered the further development of polymers like poly(alkyl thiophene) (P3HT).³ The potential of organic electronics is demonstrated by the ability of functional organic molecules called organic semiconductors to transport charge carriers.⁴⁻⁵

Organic semiconductors have unique properties⁶. These materials can function as semiconducting materials and have the chemical and mechanical virtues of organic compounds⁷. Therefore, tuning the properties of these materials can be synthetically tailored⁸⁻⁹. These materials support largely to manufacture of robust, lightweight, flexible thin films. Organic semiconducting materials are used in optoelectronics devices including transistors, light-emitting diodes, and photovoltaic cells for the application of making displays, sensors, imaging, and radio frequency identification (RFID) tags. The research expansion in the field of organic semiconductors has enabled us to explore it in more depth. The constant surge of ideas toward innovation has resulted in a large industry of organic semiconductors involved in making present and future-generation devices.

1.1. Thesis Outline

The electronic properties of the devices made of semiconducting devices depend on a variety of factors including thin film morphology. Organic semiconductor morphology is strongly influenced by the deposition technique used to create thin films. There are many deposition techniques for making films of organic semiconductors like thermal evaporation, drop-casting, spin-coating, slot-casting, spray-coating, screen printing, inkjet printing, and many more. Some are shown in figure 1.1. Depending upon the types of materials and application the optimal deposition condition can vary.

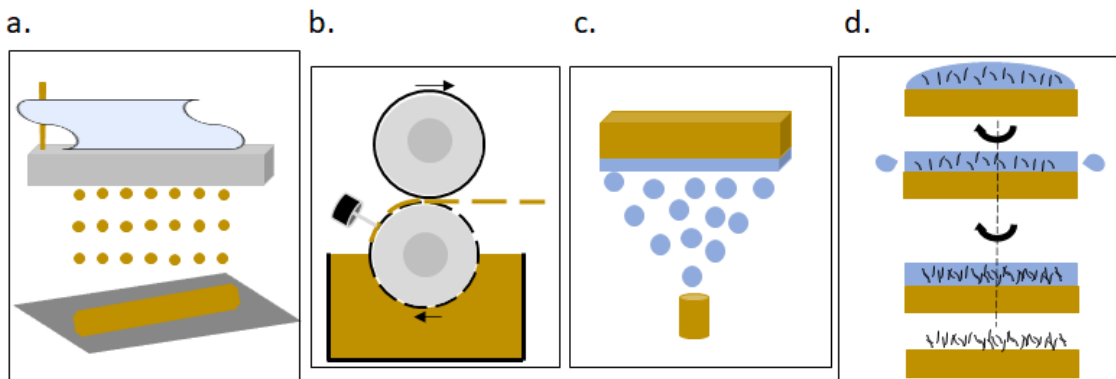


Figure 1.1. Deposition techniques (a) Inkjet Printing (b) Gravure Printing (c) Vacuum Deposition (d) Spin Coating

Almost every deposition technique has some limitations. That is why new techniques are diligently being explored. This thesis revolves around a novel supercritical fluid deposition technique¹⁰. It is a solution-based film deposition technique that leverages the solubility properties of organic electronic materials in the supercritical fluid region of the phase diagram.

In the case of supercritical fluid, there is no distinguishable phase boundary between liquid and gas¹¹. The degree of gas-like versus liquid-like behavior is strongly influenced by the fluid temperature and pressure. Thus, by altering the temperature and pressure of supercritical fluids, significant changes in the solubility properties of the polymers can be achieved. The deposition technique relies on these modulations.

The important concepts that play a direct or indirect role in the supercritical fluid deposition of semiconducting polymer specifically, poly 3-(hexylthiophene) (P3HT) will be discussed in chapter 1. The basic principles and workings of the instruments used in this research are discussed in chapter 2. In addition, the chemical structure of the solvent and its ability to be used for p-SFD are scrutinized in Chapter 3. Chapter 4 looks ahead to future experiments including field effect transistor studies on the deposited films and substrate effects on film formation.

1.2. Structure

1.2.1. Background

In the 20th century, the field of science experienced some remarkable advancements in theory and experiments, specifically concerning the quantum theory of matter¹². Starting from the discovery of electrons, Planck's quantum theory, the atomic nucleus by Rutherford, Bohr's theory to the introduction of quantum mechanical theory defined a whole new era for the scientific ascent. The foundation of the ideas of orbitals and electronic configurations made a significant impact in this area.¹³

Atomic orbitals

According to classical mechanics, the electrons in atoms are present in certain stationary states¹⁴. Each state has a definite energy and the electrons revolve around the nucleus with a quantized angular momentum. Quantum mechanics define the electrons to no longer be in well-defined orbital motion. Instead, the electrons are subjected to follow the quantum mechanics rule and are described by three-dimensional orbitals¹⁵. The orbitals are mathematically derived regions of space with different probabilities of having an electron¹⁶.

There are four quantum numbers that describe the position and energy of the electron in an atom¹⁷. The principal quantum number(n), specifies the energy of the electron and the size of the orbital. The azimuthal quantum number (l), specifies the shape of an orbital with a specific principal quantum number. It also describes the magnitude of the angular momentum of the electron and that is why it is also known as the angular momentum quantum number. The magnetic quantum number (m_l), specifies the orientation in space of an orbital at a given energy and shape. The spin quantum number(m_s) specifies the orientation of the spin axis of an electron. According to the Pauli exclusion principle, each electron has an exclusive set of quantum numbers¹⁸.

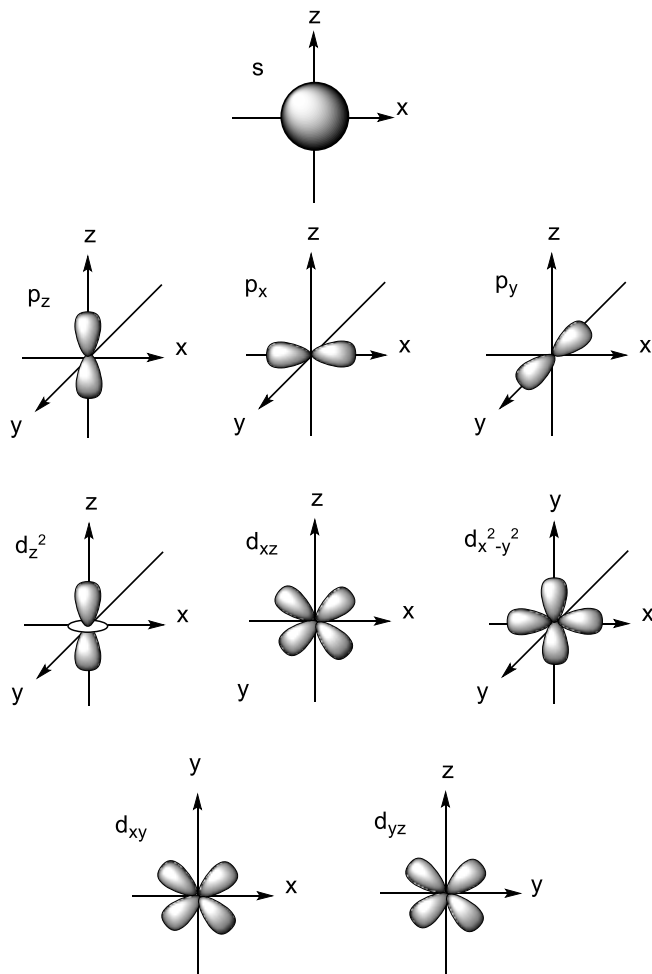


Figure 1.2. Shapes of s,p, and d atomic orbitals

Molecular orbitals

F. Hund and R. S. Mulliken developed the molecular orbital theory (MOT) at the beginning of the 20th century¹⁹. They described the structure and properties of different molecules. Molecular orbitals are the orbitals that are formed by the combination of atomic orbitals. The MOT paves the path for chemical bonding. Depending upon the interaction between the atomic orbitals, the bonding between molecular orbitals is established. Figure 1.3. shows the formation of bonding and antibonding of π molecular orbital by the interaction of atomic orbitals. The energy of combining orbitals, symmetry about the molecular axis, and extent and type of overlap between the orbitals are some of the deciding factors for the formation of molecular orbitals. The interaction between the atomic orbits can be constructive and destructive, further deciding whether the molecular orbitals

are bonding or antibonding. The antibonding orbitals are denoted by an asterisk symbol next to the associated kind of molecular orbital (σ^* , π^*). The bonding molecular orbital has lower energy and therefore greater stability as compared to that of the combining atomic orbitals²⁰. Consequently, the probability of finding the electron in the internuclear region increases in bonding molecular orbital than the combining atomic orbitals.

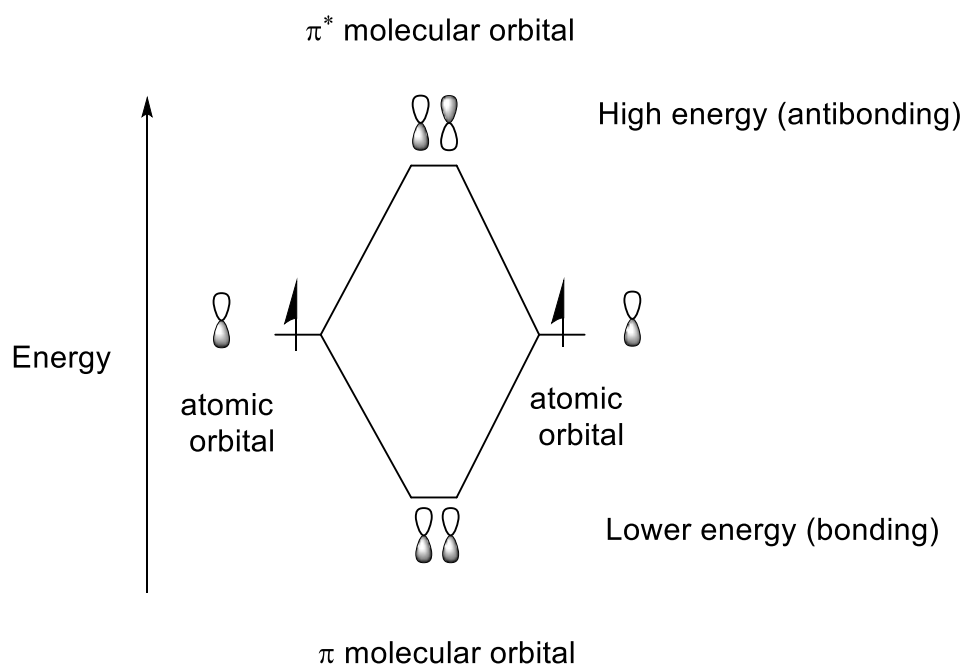


Figure 1.3. Formation of Bonding and Antibonding molecular orbitals by the interaction of atomic orbitals.

1.2.2. Organic Semiconductors

The term *organic semiconductors* refer to materials mostly made up of carbon and hydrogen atoms, often containing a few heteroatoms like sulfur, oxygen, and nitrogen. The crucial feature in these materials is the presence of conjugation along the molecule or polymeric backbone²¹. Conjugation is described as a situation that occurs when a continuous series of alternating double bonds run along the molecule²². These materials are π -bonded molecules that have repeating single and double bonds in their network of sp^2 -hybridized carbon atoms²³. The remaining p orbitals result in delocalized electrons. Figure 1.4. shows delocalization of π electrons in benzene.

The unique properties of these materials are because of the carbon atoms that can form chains, rings, or branches with the help of covalent σ or π bonds. The σ bonds are

formed between the adjacent atoms by 2s-2p hybrid orbitals. These bonds are most likely localized and comparatively stronger as compared to the π bonds. Due to their high strength, the electronic excitation energy becomes high and the optical band gap energy lands in the much higher range of visible energy range which is why the materials that are produced out of it are transparent or have no color.

On the other hand, the π bonds are formed by the overlap between $2p_z$ orbitals of adjacent atoms. These π bonds are weaker in strength than σ bonds. Also, π bonds are widely delocalized along the $2p$ orbitals of atoms that are aligned in parallel as shown in figure 1.4.

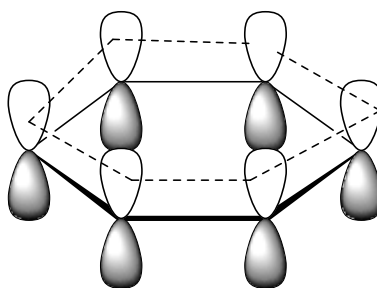


Figure 1.4. Delocalization of π electrons in Benzene

With the increase in the size of molecules the extension of delocalized π electrons increases, leading to a further decrease in electronic excitation energy and a lesser optical band gap²⁴. This allows the molecules to absorb in the visible range and therefore the materials formed are usually colored. With the increase in conjugation length, the number of states increases in the highest occupied molecular orbital (HOMO) and lowest unoccupied molecular orbital (LUMO) resulting in a higher energy difference between the two molecular orbitals²⁵. Figure 1.5. illustrates energy-level splitting in alkenes shows increasing conjugation length leading to a decrease in the energy between HOMO and LUMO.

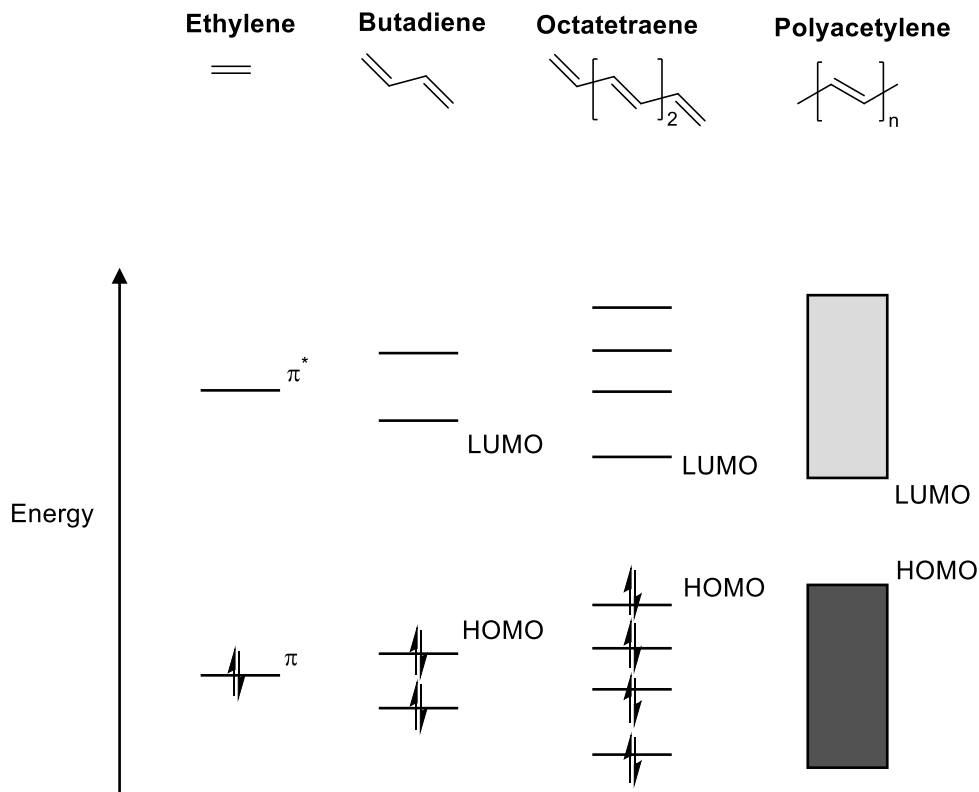


Figure 1.5. Energy-level splitting in alkenes with increasing conjugation length

1.3. Doping in Organic Semiconductors

Like inorganic semiconductors, the conductivity of organic semiconductors can be modulated by doping²⁶. Doping is a method of introducing impurities in materials for modulating their optical, electrical, and structural properties. It has led to the development of semiconductor technology through the formation of pn junctions, for example. Initial studies show that the basic concept and methods of doping in organic semiconductors are similar to inorganic semiconductors²⁷. Therefore, doping was initiated in organic molecules containing strongly oxidizing gases and then on small atoms or molecules. These studies displayed accomplishment of high conductivities in them²⁸. However, the propensity for the small dopants to diffuse within the organic layer led to device instability²⁹. Therefore, more coherent approaches to doping have been a subject of research in the last few years. Predominantly doping can be achieved from the injection of charges at electrodes, intended or accidental doping, or dissociation of photogenerated electron-hole pairs that are bound together by coulomb attraction³⁰. Figure 1.6 describes p-type and n-type doping

in an organic semiconductor. In p-type doping, the dopant acts as an electron acceptor whereas in n-type, the dopant acts as an electron donor.

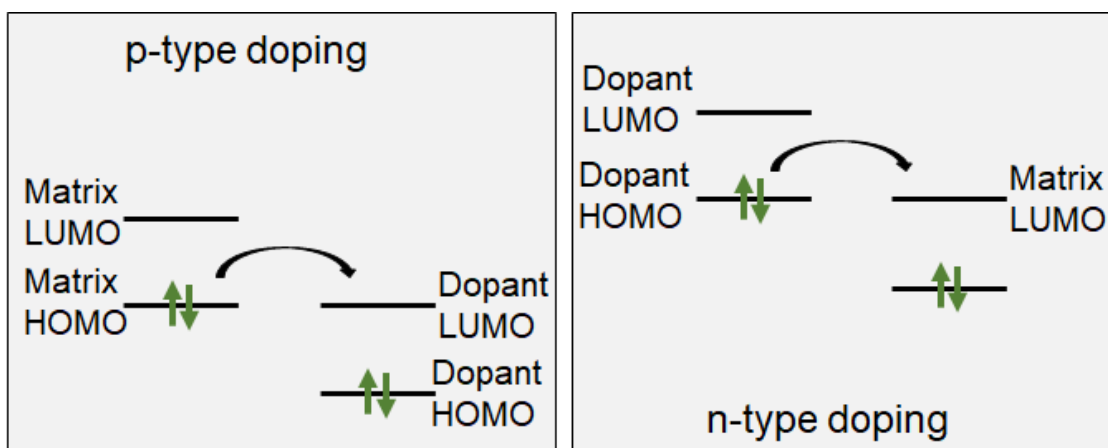
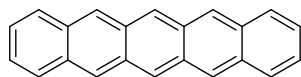


Figure 1.6. p-type and n-type doping in organic semiconductor

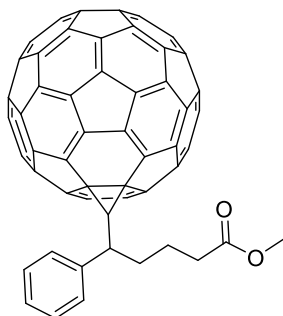
1.4. Types of Organic Semiconductors

Organic semiconducting materials can broadly be divided into two main categories; small molecules and polymers³¹. These two types of materials have preeminent differences in them. Usually, Small molecules are lower molecular weight organic molecules that are deposited using vapor deposition techniques³². Alternatively, semiconducting polymers have high molecular weight and cannot be deposited through sublimation under a vacuum. The polymer films are often disordered, forming crystalline and amorphous regions³³. In addition, the connectivity between crystalline domains required for high conductivity was shown not to occur in low molecular weight polymers, affecting their charge carrier transport by several orders of magnitude³⁴. The term “small molecule” in the organic semiconductor community is something of a misnomer as the number of atoms frequently exceeds fifty³⁵. With respect to their thin film morphology, small molecules tend to be more crystalline with a higher order as compared to polymers. On contrary, semiconducting polymers are long chains of repeating monomer units often with aliphatic side chains attached to them³⁶. These flexible side chains are an important part of semiconducting polymers as they dramatically increase solubility and ordering within the film, the latter is responsible for higher mobility. Figure 1.7 and figure 1.8 shows structures of some commonly used organic small molecules and polymers.

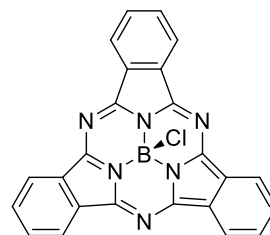
Small Molecules



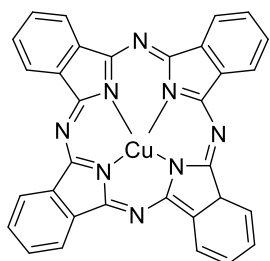
Pentacene



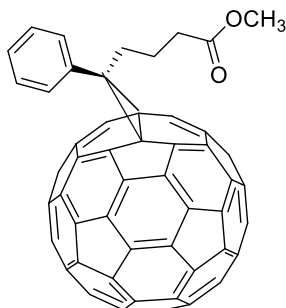
[6,6]-phenyl-C61-butyric acid methyl ester



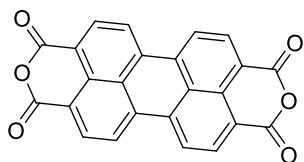
Boron subphthalocyanine chloride



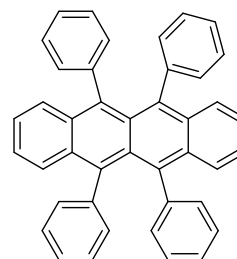
Copper(II) Phthalocyanine



[6,6]-phenyl-C71-butyric acid methyl ester



Perylenetetracarboxylic dianhydride



Ruberene

Figure 1.7. Structures of small molecules

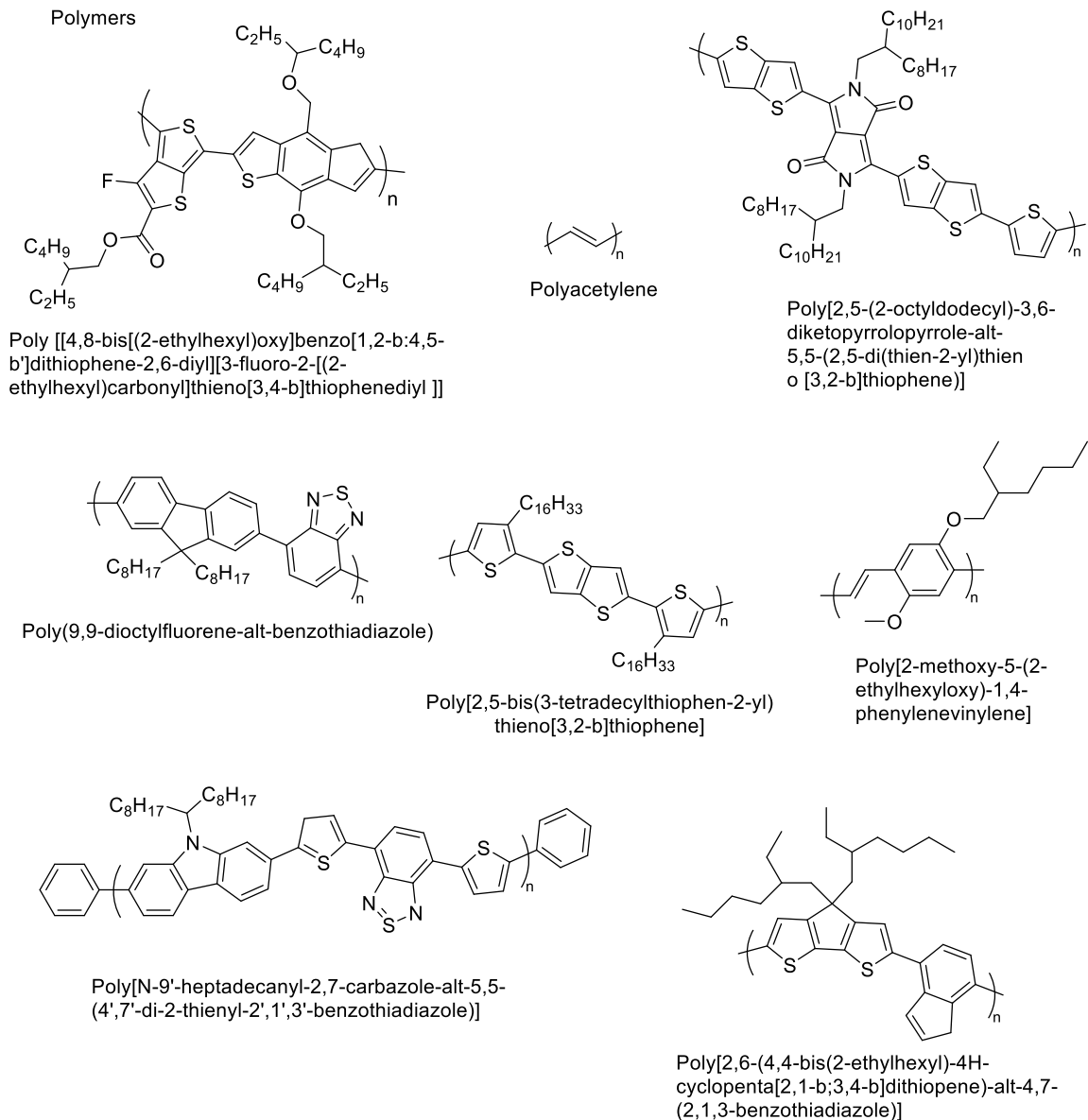


Figure 1.8. Structures of organic semiconducting polymers

1.5. Charge Transport Mechanisms

Several factors are responsible for charge carrier transport including the structure and molecular geometry of the materials as organic semiconductors are proportionally disordered. For that reason, concepts from disordered semiconductor theory are often invoked³⁷. In addition, the charge carriers are not as delocalized as they are in inorganic semiconductors, leading to the idea that electronic-vibrational rearrangement is important

during charge motion³⁸. However, the mobility of charge carriers in organic semiconductors can vary by many orders of magnitude depending on the compound in question³⁹. Hence, currently, there is no entrenched charge carrier transport mechanism for organic semiconductors, it remains an open line of inquiry⁴⁰. Some concepts relevant to charge transport are discussed below.

1.5.1. Band Structure

Typical inorganic solids are composed of tightly packed molecules that are present in exceedingly higher numbers as compared to other states of matter. This leads to the formation of an exceptionally large number of states with a small energy difference between them. Therefore, these states are often contemplated as energy bands rather than discrete energy levels⁴¹. An energy band contains so exorbitant number of continuous energy levels that nearly reaches a continuum. Nonetheless, few bands are broadly segregated forming band gaps. The gap between the bands' changes depending on the bond strength and crystal structure⁴². The highest energy band that is filled with electrons is known as the valence band whereas the lowest unoccupied energy band is known as the conduction band. Insulators have the highest band gap whereas semiconductors have a smaller energy gap. However, the difference between a wide-bandgap semiconductor and a narrow-bandgap insulator is somewhat subjective. Thus, the distinction between semiconductors and insulators is qualitative and can depend on context. In metal, there is an overlap between the valence and conduction bands, such that one typically does not use the terminology of valence and conduction bands. Instead, the dividing line between occupied and unoccupied states, called the Fermi Level, is the main way of describing the electronic structure of metals as shown in figure 1.9. The fact that metals have zero energy bandgap is responsible for their ability to conduct charges, even at absolute zero⁴³.

In organic semiconductors, the simple band transport picture is not considered a complete description of the charge carrier transport mechanism. Molecules like rubrene have high mobility and have been demonstrated to show the Hall effect, a classic demonstration of coherent transport⁴⁴. However, the interaction of mobile charge carriers with the molecular degrees of freedom can cause the carrier to localize in a way inconsistent with the typical band theory that governs charge transport in inorganic semiconductors.

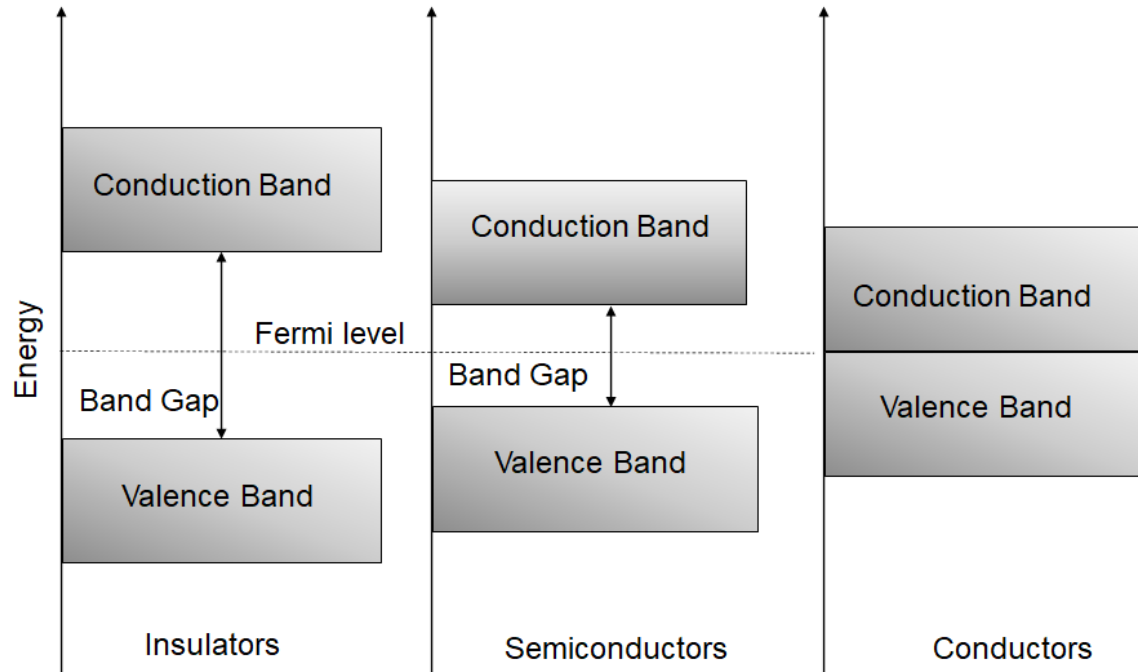


Figure 1.9. Band gap in conductor, semiconductor, and insulator

1.5.2. Disordered-based Mechanism

In the case of strong charge carrier localization, the transport mechanism can be thought of in terms of hopping between sites that can accept an electron or hole. Localized charge carriers distort the underlying lattice, forming a polaron⁴⁵. In this mechanism, the charge carriers along with their underlying lattice distortion move from one site to another in a mechanism called charge carrier hopping⁴⁶. The movement of charges is thermally activated, with increases in temperature leading to increased mobility.

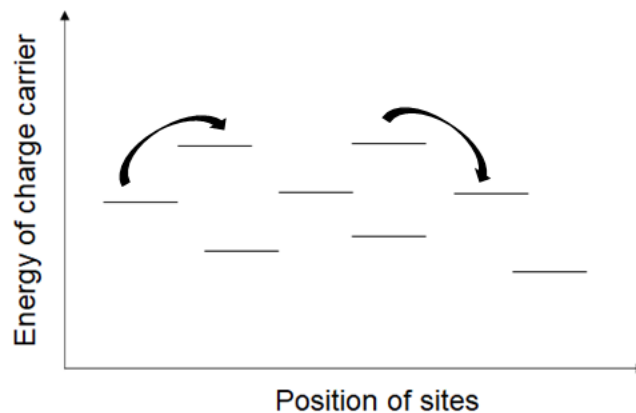


Figure 1.10. Hopping transport between localized state

1.6. Impact of Structure on Charge Transport

The high molecular weight molecules have defects present in them. The presence of defects leads to an obstruction in the overlapping of neighboring p-orbital which cause discontinuity in conjugation. These molecules contain segments of conjugation that are separated by insulating grain boundaries.

1.6.1. Regioregularity

One of the major factors that influence the charge transport characteristics in semiconducting polymers is regioregularity⁴⁷. Regioregularity is the percentage of head-to-tail interconnections with the repeating units. Regioregular semiconducting polymers follow a strict orientation of alternating asymmetric repeating units throughout the polymer backbone. The arrangement of alkyl chains to the polymer backbone can have three configurations: head-to-tail (HT), head-to-head (HH), and tail-to-tail (TT). Figure 1.11 shows HH, HT, and TT configurations on P3HT. In the case of a regioregular arrangement, the alkyl groups are arranged in a repeating pattern of specific configuration. However, in the case of regiorandom arrangement, there is no specific pattern of alkyl groups. Figure 1.12 shows regioregular and random P3HT.

Regioregular P3HT (>90%) has higher crystallinity with lamella packing with edge-on orientation to the substrate and finer π -stacking as compared to amorphous P3HT whereas regiorandom P3HT (~80%) contains irregular conformation with poor packing with face-on orientation to the substrate and lower crystallinity⁴⁸.

1.6.2. Molecular Weight

Semiconducting polymers are long repetitive chains of monomers. The longer chains signify the higher molecular weight of polymers. The length of polymer chains determines the strength and solubility properties of polymers⁴⁹. The polymers do not have solitary molecular weight because of the different unequal chains present in them.

Therefore, a distribution of polymer chains and molecular weights are averaged. Hence, the molecular weight of polymers is evaluated by the average molecular weights.

Number Average Molecular Weight

The number average molecular weight is denoted by M_n . It is the average of the molecular weights of all the polymer chains. M_n is given by,

$$M_n = \frac{\sum N_i M_i}{\sum N_i} \quad 1.1$$

Where M_i is the molecular weight of the polymer chain, N_i is the number of chains having the same molecular weight.

Weight Average Molecular Weight

The weight average molecular weight is denoted by M_w . It is the average of the weights of molecular weight of the polymer chain. M_w is given by,

$$M_w = \frac{\sum N_i M_i^2}{\sum N_i M_i} \quad 1.2$$

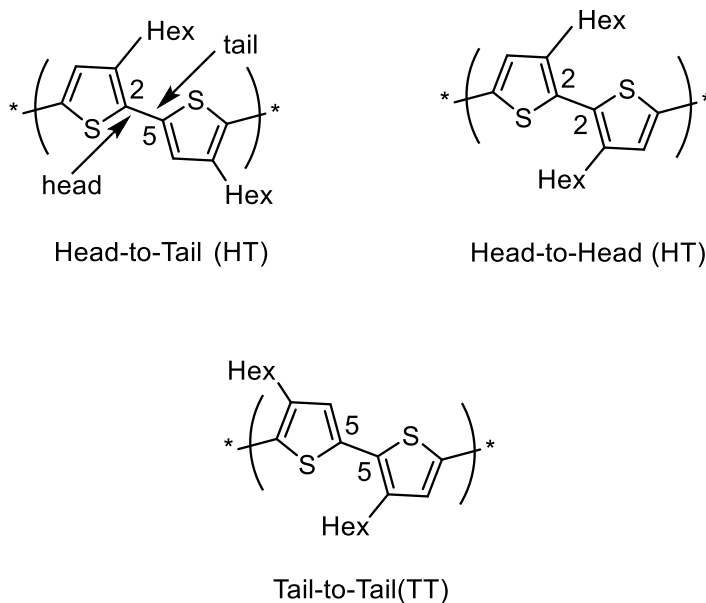


Figure 1.11. HH, HT, TT in P3HT

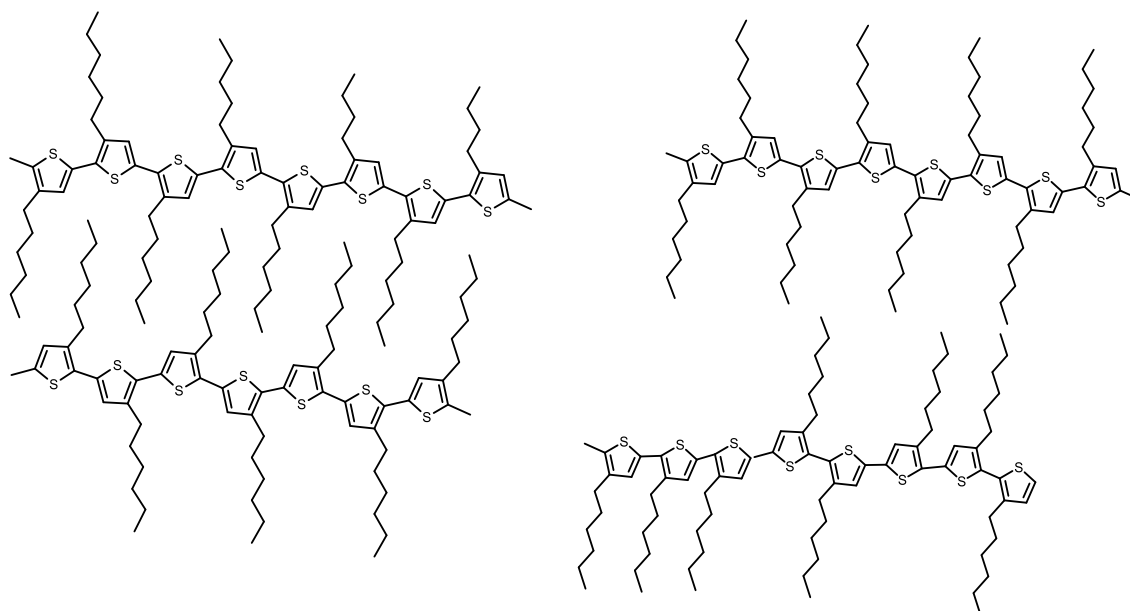


Figure 1.12. Regioregular (left) and regiorandom (right) P3HT

Polydispersity Index

The polydispersity index is the ratio of M_w to M_n . It helps measure the extent of distribution of the molecular weight of the polymer. In the case of semiconducting polymers, it has been generally observed that the lower molecular weight polymers are more ordered often showing higher crystallinity in their structures thereby affecting the charge carrier transport in them⁵⁰.

The molecular weight has a profound effect on the charge carrier transport mechanism⁵¹. The films made of low molecular weight have a higher degree of crystallinity as compared to that of high molecular weight films. In high molecular weight films, the effect of insulating grain boundaries is reduced by bridging between the neighboring grains.

1.7. Supercritical fluid

Supercritical fluids are the substances above that have a temperature and pressure above their critical value⁵². The temperature corresponding to the critical point is known as critical temperature denoted by T_c and the pressure corresponding to the critical point is known as critical pressure denoted by P_c . There is no distinguishable phase boundary present in this region⁵³. As a result, fluids in the vicinity of the critical point have

many of the typical properties of supercritical fluids, namely the combined characteristics of liquid and gas which are tunable with pressure and temperature. More specifically, supercritical fluids exhibit gas-like viscosities and liquid-like densities⁵⁴. In addition, at the critical point, the compressibility of fluid becomes nearly infinite. These are the properties that are taken advantage of for our film deposition process. Figure 1.13 represents the pressure-temperature phase diagram in which the curve separating the liquid and gas phase ends at the critical point then the phases disappear to form the supercritical fluid phase and figure 1.14. illustrates the phase transition in the supercritical fluid. Figure 1.14 (A) shows distinct liquid and gas phases. (B) and (C) show distinguishable liquid and gas phases (D) shows the two phases become indistinguishable.

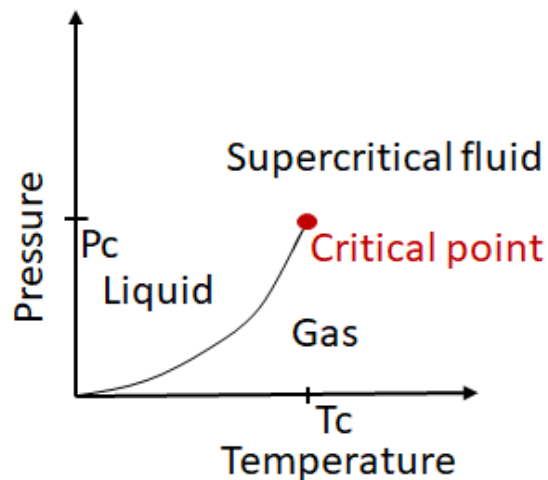


Figure 1.13. Phase diagram showing the supercritical fluid region

The perfect gas law is the approximate equation of the state of any gas when the density of the gas is very low, meaning that the size of the gas atoms or molecules can be neglected, as can the forces between them. This law is a combination of several gas laws such as Boyle's law ($PV = \text{constant}$, at constant n , T); Charles' law ($V = \text{constant} \times T$, at constant n , P and $P = \text{constant} \times T$, at constant n , V) and Avogadro's principle ($V = \text{constant} \times n$, at constant P , T). The perfect gas law is given by,

$$PV = nRT \quad 1.3$$

Where P is pressure, V is volume, n is the number of moles, T is temperature, and R is the universal gas constant.

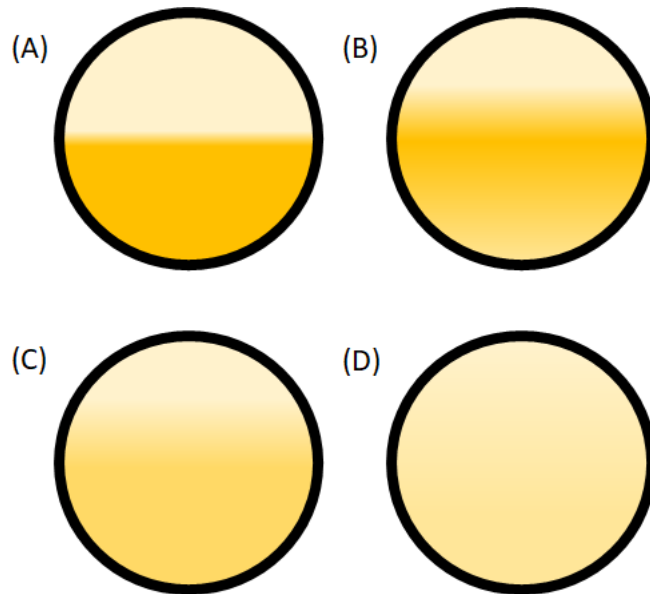


Figure 1.14. Phase transition in supercritical fluid (A) two distinct phases (liquid and gas) (B) the phases start to diminish (C) liquid and gas phases become more similar (D) liquid and gas phases become indistinguishable.

The van der Waals equation is a model equation of state for a gas that includes molecular attractions and repulsion as well as the finite size of the gas atoms or molecules. This equation captures the general features of the behavior of many real gases. The van der Waals equation is given by,

$$P = \frac{nRT}{V - nb} - a \frac{n^2}{V^2} \quad 1.4$$

The constants a and b are known as van der Waals coefficients. a is related to the strength of forces of interactions, and b is related to the excluded volume.

As shown in figure 1.15, the isotherm has different shapes, which are determined by temperature value. When temperatures are lower than critical temperature ($T < T_c$), the pressure decreases with increasing volume. The isotherm passing through the critical temperature ($T = T_c$) helps to determine the conditions for phase transition. As the temperature increases beyond critical temperature, the isotherms become straight lines with decreasing volume ($T > T_c$). This indicates the coexistence of two phases. When the

gas is compressed, the pressure increases until point a. Further compression does not lead to a pressure increase. Between points a and b, the gas and liquid phases coexist. After complete liquefaction (at point b) even a slight increase in volume results in a rapid increase in pressure.

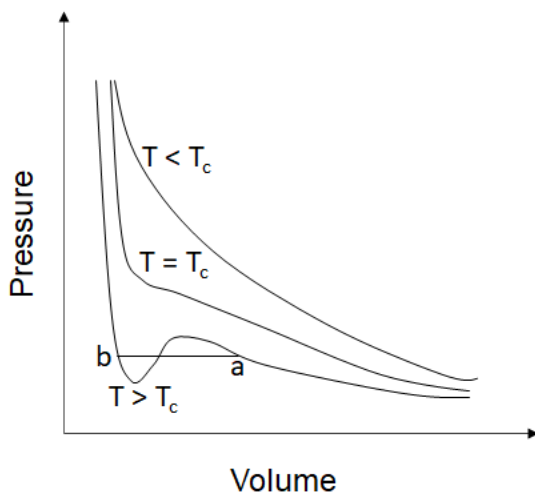


Figure 1.15. Isotherms showing van der Waals equation of state

1.7.1. Gibbs Free Energy

Gibbs free energy furnishes the requisites for chemical reactions. Thermodynamically a spontaneous process at constant temperature and pressure is described by a decline in the Gibbs free energy. The Gibbs free energy of mixing, ΔG_m is given by,

$$\Delta G_m = \Delta H_m - T\Delta S_m \quad 1.5$$

Where, ΔH_m is the change in enthalpy of mixing, T is temperature, ΔS_m is the change in entropy of mixing.

The Gibbs free energy equation helps to discover the conditions for a chemical reaction⁵⁵. The negative value of ΔG_m implies that the reaction is spontaneous meaning a thermodynamically favorable process.

1.7.2. Flory Huggins Theory

The Flory Huggins (FH) model is the most popular model for describing polymer solutions⁶⁰. Figure 1.16 represents the lattice model of a polymer solution where the polymer and the solvent occupy the lattice sites⁶¹. The black ones represent the lattice sites filled with polymer and the rest of the lattice sites are of solvent. The FH theory is relatively crude, but it exhibits a fundamental insight into polymer mixing behavior. It can be considered the polymer counterpart of a regular solution theory. However, this is more complicated because polymers are long chains of monomers. The differing molecular sizes present in a polymeric molecule decrease the entropy of mixing in the solution relative to a solution of monomers only. In addition, FH theory describes the interaction between the segments of the polymer chains. This interaction parameter is represented as, χ . The Gibbs free energy of mixing obtained from Flory Huggins is given by,

$$\Delta G_m = -RT[x_1 \ln \phi_1 + x_2 \ln \phi_2] + RT\chi x_1 \phi_2 \quad 1.6$$

Where x_1, x_2 represent mole fractions and ϕ_1, ϕ_2 represent volume fractions of solvent and polymer.

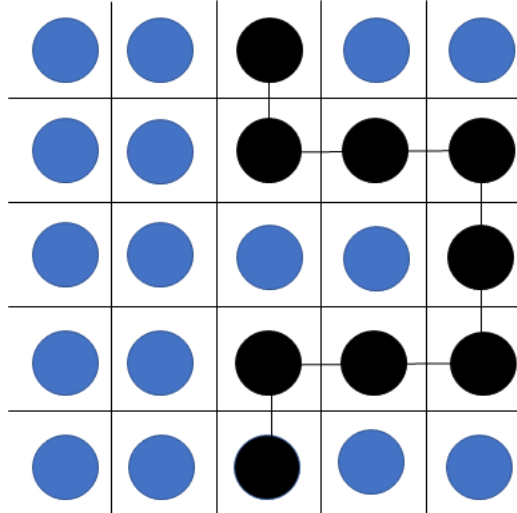


Figure 1.16. Lattice model of a polymer solution

1.8. Fluid Flow

An understanding of fluid mechanics has proven necessary for understanding the process of supercritical fluid deposition and self-assembly⁶². This is, in part, due to the fact that the viscosity of the fluid is very low while the compressibility is very high⁶³. As a result,

fluid flows in supercritical media can be highly complex, and affect the pre-aggregation step necessary for polymer deposition in supercritical fluids where pre-aggregation refers to self assembly of material in solution prior to deposition on substrate.

1.8.1. Rayleigh Number

The buoyancy-driven flow in a fluid is given by the Rayleigh number (Ra)⁶³. The Rayleigh number explains the fluid flow by considering several factors responsible for it. The Rayleigh number is given by,

$$Ra = \frac{g\beta\Delta TL^3}{\nu\alpha} \quad 1.7$$

In eq. 1.7 g is the acceleration due to gravity, β is the thermal expansion coefficient, ΔT is the temperature difference, L is the length, ν is the kinematic viscosity, and α is the thermal diffusivity.

The Rayleigh number gauges the effects of important factors attributing to the flow of a fluid. It is given by measuring the influence of gravitational force, buoyancy forces, viscosity, thermal conduction, and diffusivity. It helps in designating different regimes in fluid flow to laminar flow and turbulent flows in the fluid. Figure 1.17 (top) shows smooth and streamlined fluid flow called laminar flow whereas the irregular and chaotic fluid flow (bottom) is turbulent flow.

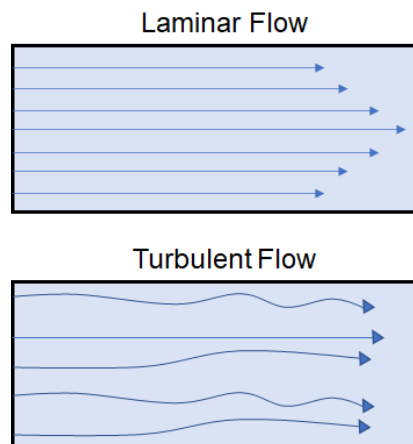


Figure 1.17. Schematic of Laminar and Turbulent fluid flow

1.9. Ultraviolet-visible Spectroscopy

Ultraviolet-visible (UV-vis) spectroscopy is an extensively used spectroscopic technique in scientific research. This technique relies on the sample to be a chromophore, i.e., it should absorb light in the ultraviolet-visible region⁶⁴. It can evaluate the wavelength in which the light is being absorbed or transmitted by the sample. In the electromagnetic spectrum, there are several regions present.

The sample molecules used in this technique absorb electromagnetic radiation in the ultraviolet or visible range. The amount of radiation or photons absorbed is expressed in terms of absorbance. When the molecule absorbs energy, an electron is excited from the ground electronic state to the excited electronic state⁶⁵. This is termed electronic transition. Electromagnetic radiation has a specific amount of energy associated with it which is given by,

$$E = h\nu \quad 1.8$$

Where E is the energy, h is Planck's constant is 6.62×10^{-34} J s and ν is the frequency.

The electrons may undergo various possible transitions of different energies. In conjugated polymer, the most important transitions are between the π bonding orbital and the π^* antibonding orbital⁶⁶.

1.9.1. Franck Condon Principle

In UV-Visible spectroscopy in the condensed phase, vibrational transitions often accompany the electronic transitions primarily responsible for light absorption⁶⁷. This results in several peaks that accompany the primary electronic transition as shown in the figure 1.18. James Franck and Edward Condon gave a rule in spectroscopy that describes the intensity distribution in vibronic transitions⁶⁸. This rule is based on the establishment of an electronic transition being much more rapid than a vibrational transition in a molecule. It states that the most significant overlap between the vibrational wave functions determines the electronic transition and generates the most intense spectral peak.

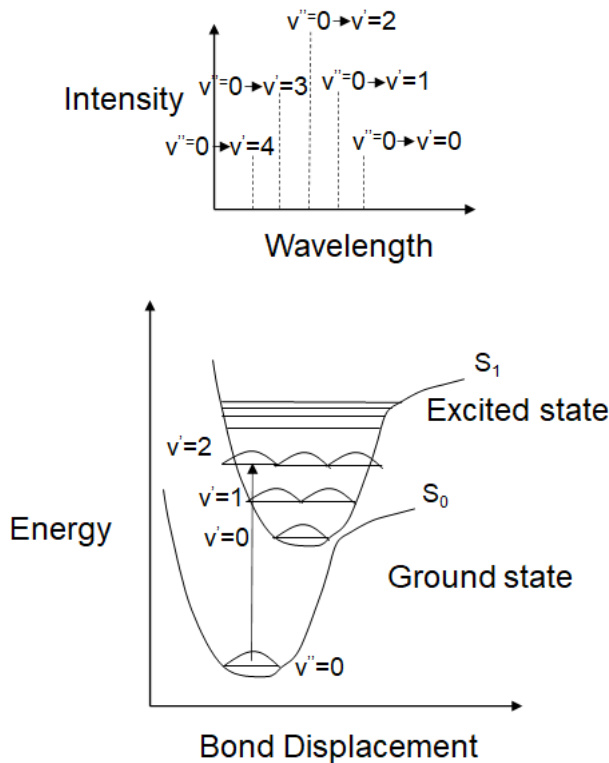


Figure 1.18. Schematic absorption spectra (top) and potential curve diagram (bottom)

Figure 1.18 (bottom) shows a potential curve diagram with the transition from the ground (S_0) to the excited electronic state (S_1). The most significant overlap is between $v''=0$ to $v'=2$ vibrational wave functions which are shown in the top figure with the highest intensity.

1.9.2. Beer-Lambert Law

UV-visible spectroscopy relies on the principle of absorption of light in the ultraviolet or visible range by the compound. The relationship between the absorbance and concentration of a solution is given by the Beer-Lambert law⁶⁹, which is expressed as,

$$A = \epsilon cl \quad 1.9$$

Where A is absorbance, ϵ is molar absorptivity, c is the concentration of the compound, l is the length of the sample cell. The molar absorptivity, ϵ , also known as the molar extinction coefficient is a property of measuring the extent of absorbance by a specific

molecule at a given wavelength. Absorbance is defined by the intensities of the incident and transmitted light⁷⁰.

$$A = \log(I_0 / I) \quad 1.10$$

Where I_0 is the intensity of light incident upon the sample, I = intensity of light transmitting (leaving) from the sample

The amount of light passing through the sample is called transmittance and is usually given by,

$$T = \frac{I}{I_0} \quad 1.11$$

$$\%T = \frac{I}{I_0} \times 100 \quad 1.12$$

1.10. Organic Field Effect Transistors

An organic field effect transistor (OFET) is a device that forms the basis of many circuits⁷¹. It consists of three main parts: the electrodes (source, drain, and gate), the dielectric layer, and the semiconducting channel⁷². The source and drain are commonly in the same plane and separated by a channel length l . The dielectric layer separates the active layer from the gate electrode. There are several configurations of OFETs possible depending upon the position of the electrodes as shown in figure 1.19.

Voltage is applied through the gate and the charge carriers get accumulated on the interface of the dielectric and semiconducting channel. The drain, source, and gate electrodes are biased to V_D , V_S , and V_G respectively. These mobile charges contribute to the current which helps in determining the conductivity of the device⁷³. OFETs can be characterized with the help of two curves: the output curve and the transfer curve. The output curves are the plot of the drain current as a function of drain voltage for different gate voltages and transfer curves are the plots of drain current as a function of gate voltage for a given V_{SD} .

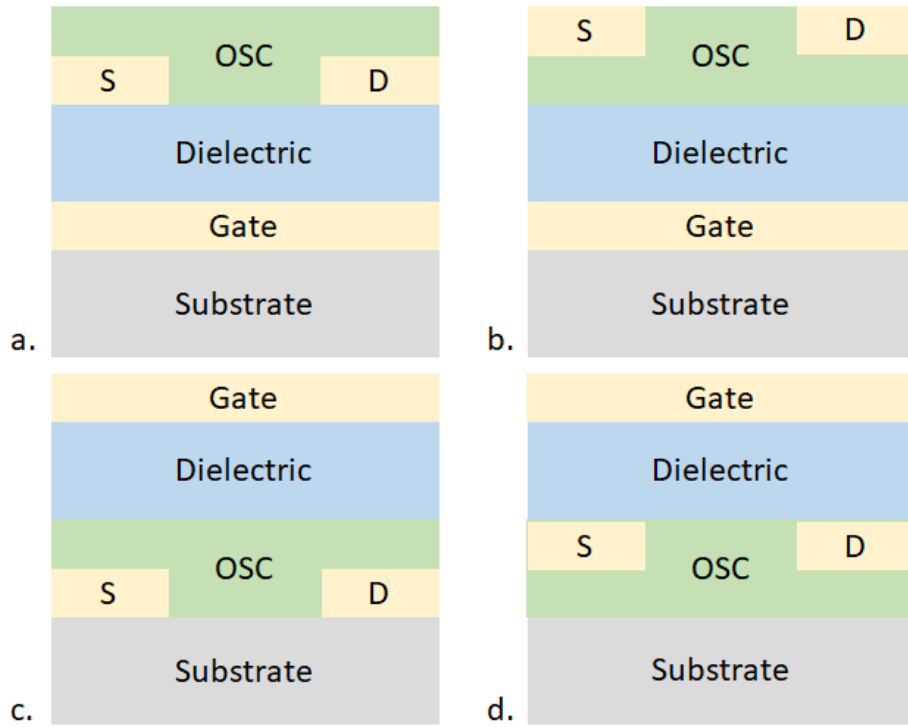


Figure 1.19. Configurations of organic field-effect transistors a. bottom gate bottom contact b. bottom gate top contact c. top gate bottom contact d. top gate top contact

The important representations in an OFET are given by the following terms: L is the channel length, W is the channel width, V_{TH} is the threshold voltage. The threshold voltage is the minimum gate voltage required for creating conducting path between the source and drain electrodes⁷⁴. The operating regimes of OFET are shown in figure 1.20. In the case of the output curve, with small V_{DS} , a linear regime is formed and further application of V_{DS} leads to a point called a pinch-off point where the depletion region is formed. Beyond this point, a saturation regime is obtained where the current remains constant.

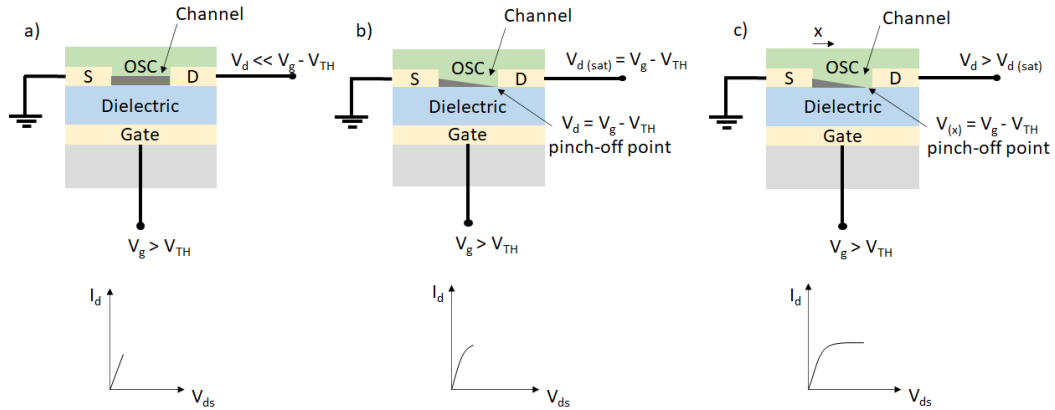


Figure 1.20. Operating regimes a) linear regime b) start of saturation regime at pinch-off c) saturation regime and corresponding current-voltage characteristics

In the case of the transfer curve, the drain current is plotted as a function of V_{GS} for a given V_{SD} . Transfer curves help in extracting the mobility (μ) of the device. For calculating mobility, from the linear regime and saturation regime the following equations are helpful⁷⁵: C_i is the capacitance. Transistor measurements are highlighted in future work section.

Linear Regime

$$I_{DS} = WC_i V_{GS} \mu \frac{V_{DS}}{L} \quad 1.13$$

$$\mu = \frac{L}{WC_i V_{DS}} \left(\frac{\partial I_{DS}}{\partial V_{GS}} \right)_{V_{DS} \rightarrow 0} \quad 1.14$$

Saturation Regime

$$I_{D(sat)} = C_i \mu_{(sat)} \frac{W}{2L} V_{GS}^2 \quad 1.15$$

$$\mu_{(sat)} = \left(\frac{2L}{WC_i} \right) \left(d \frac{\sqrt{I_{D(sat)}}}{V_{GS}} \right)^2 \quad 1.16$$

In an organic field effect transistor, contact problems, the presence of traps in semiconducting materials, surface roughness, contact resistance, and leakage current (charge carriers in dielectric or semiconductor) are some of the reasons for not getting a perfect device. Some of the observed behaviors for poor devices that are evident from current vs voltage plots include non-linear behavior in the linear regime, presence of hysteresis, threshold and turn-on shift with the application of V_{SD} or V_G , and gate voltage-dependent mobility.

In conclusion, several key aspects of chemical bonding necessary to understand the properties of organic semiconductors have been presented. Their structures contain an extended pi-conjugated network as shown in several examples. The thesis will demonstrate the deposition of one polymer semiconductor using p-SFD which leverages the properties of supercritical fluids. The technique also relies on an understanding of polymer solubility. Future work will use field effect transistor measurements, which were also discussed.

Chapter 2. Methods

2.1. Supercritical Fluid Chamber

All the material solubility experiments and film deposition are done in a custom-made supercritical fluid chamber. The whole setup of the SCF chamber is done in a well-ventilated area of the lab. The SCF chamber is made up of copper beryllium. Copper Beryllium is used for its high strength, high thermal conductivity, non-sparking, and non-magnetic features. The chamber exterior is in the shape of a cube with an internal volume of around 30 mL. The chamber has six ports. Each port is covered using a flange made of copper beryllium. The thickness of the flange is 10 mm, the outer diameter is 60 mm and the inner diameter is 20 mm. It can withstand a maximum of 7700 psi pressure. A rupture disc of 7700 is used to protect against overpressure in the SCF chamber. A rupture disc is a safety device that has a specific breaking point in response to a particular pressure and is often used for pressure relief applications. The chamber has two sapphire windows (Al_2O_3) on opposite sides which helps to collect in-situ transmission UV-Visible spectra. They are used because of their transparency-to-light feature. The diameter of these windows is 1.14 inches and the thickness is 0.29 inches. The pressure rating of the windows is 130000 psi making it probably the strongest part of the chamber. However, the pressure rating of the windows decreases dramatically in the presence of cracks and chips, so the windows must be inspected regularly. On the other hand glass of the same dimensions has a yield strength of 12510 psi which is almost 10 times weaker than that of sapphire. Copper gaskets are placed between the flange and the windows to provide extra thickness so that windows can be held by the flanges. Copper is also softer than BeCu, making it less likely to damage the windows. For covering the ports of the chamber, caps made of stainless steel (316) of diameter 28 mm and 5 mm thick are used. The yield strength of the 316 stainless steel cap is more than double the maximum working pressure. The fluid caps are connected to a Swagelok T SS-200-3-4TMT fitting. This fitting has three connection points, one National Pipe Thread (NPT), designed to interface with the SS caps, and two Swagelok connections that form connections to 1/16" SS tubing. Teflon tape is used around the NPT connections. Teflon starts to decompose around 260 °C and decomposes completely above 360 °C⁷⁶. Thermally, Teflon tapes are the weakest point of the chamber. In case of overheating, the Teflon tapes will break and the system will be unable to hold pressure. The pressure will start decreasing rapidly. The flange is

tightly sealed using 12.9-grade steel bolts (M50.8×20mm, ASTM F569M by HOLO-KROME®). These bolts have a tensile strength of 176946 psi and a tensile strength area of 14.2 mm². Because there are six bolts, the yield strength of the assembly exceeds six times the yield strength of the bolt times a 0.75 safety factor. To seal the chamber, the bolts must be tightened securely. To ensure sufficient bolt tightness without overtightening, a 65 ft/lbs torque wrench is used to tighten the bolts. The steel bolts have low machinability, weldability, and formability. Due to this, they are replaced with new ones regularly after every 8-10 runs. In addition, the chemical potential difference between the steel bolts and the BeCu chamber housing causes corrosion of the bolts. To circumvent this issue an attempt to use more chemically resistant titanium bolts was also made. However, the bolts were unable to withstand the torque applied during chamber assembly, as such, the original steel bolts are still in use. Thermal paste is applied around the bolt threads to allow smooth grooving of bolts. It is also a good thermal conductor and helps in creating a tight seal allowing a better rate of heat transfer through the bolts.

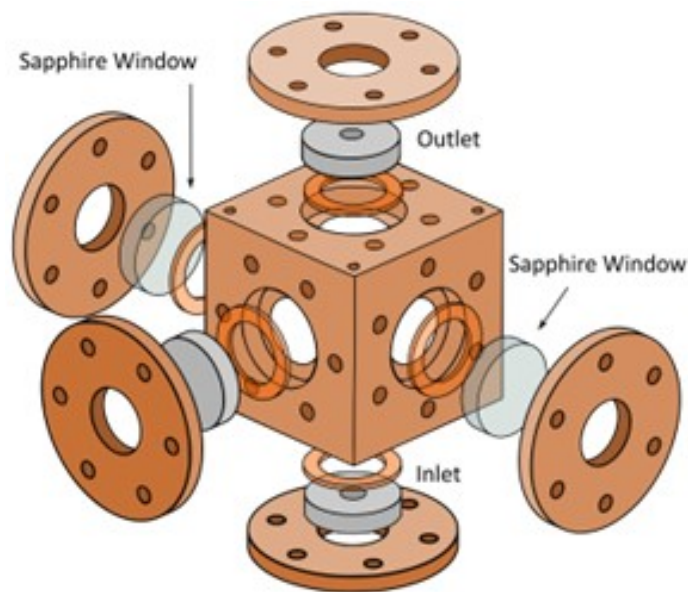


Figure 2.1. Drawing of the supercritical fluid chamber

Different types of tubing and fittings are used in the chamber to connect with its different components. Vacuum tubing is used for connecting the chamber body to the cold trap. Feed1/feed2 are connected to the solvent bottle using stainless steel tubing. A relief valve with relief set to 10 psi is used. The final assembled chamber is rated to 7700 psi. The pressure rating is limited by ½" male NPT connectors that are attached to the valves.

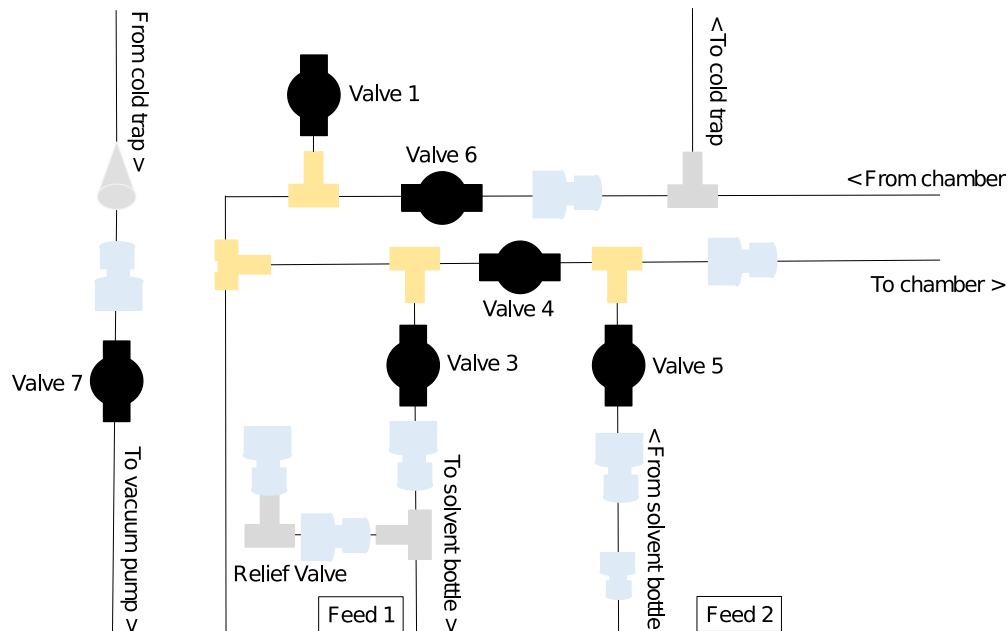


Figure 2.2. Overview of gas manifold

The inlet and outlet ports are present at the top and bottom of the chamber respectively to allow complete filling and emptying of the chamber.

The SCF chamber is assembled, and the digital pressure transducer is plugged in. The pressure generator is fully retracted. Any visible leaks after proper tightening of the fittings are checked using Snoop. Snoop is a leak detector that is commonly used in pressurized gas systems. Bubbles are generated in the place of leaks after applying Snoop generously to the chamber, needlepoint valves, and Swagelok fittings.

The assembled chamber is placed inside a Lexan safety enclosure. Lexan is a polycarbonate, thermoelastic polymer which is prominently known for its low weight and high impact resistance often considered 'virtually unbreakable.' However, it is not chemical resistant and is scratchable. When heated solvents come in contact with Lexan, they often soften the outermost surface. Solvents like toluene, benzene, and acetone are some of those solvents. The melting point of Lexan is around 300 °C which is much higher than the highest set temperature of the SCF chamber.

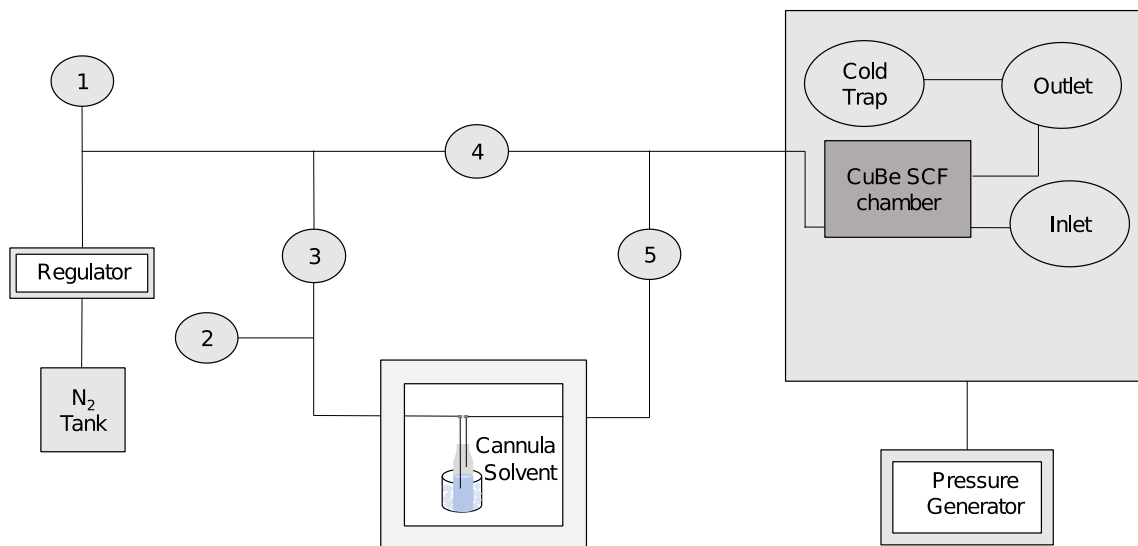


Figure 2.3. Overview of pipes and valves of the SCF chamber

2.2. Experimental Procedures

A glass crucible is filled with the semiconducting polymer and placed inside the bottom of the chamber. The filled crucible is covered with cotton wool and porous copper mesh to avoid any unconstrained dispersal of polymer inside the chamber.

Important preliminary checks are done before filling the solvent in the chamber. The digital temperature controller should be set to off and the pressure indicator should read zero. Also, it is crucial to check whether there is sufficient solvent in the solvent bottle for filling the SCF chamber. Moreover, the solvent bottle should be adjusted such that the cannula connected to valve 5 is at the bottom of the bottle and the cannula connected to valve 3 is at the top as shown in the Figure. 2.3.

The nitrogen gas cylinder is then turned on for the purging of the chamber. In order to do that first, it is important to ensure that valves 3 and 4 are closed. The outlet regulator valve should be closed as well. Now, the main regulator valve is opened and valve 1 is slightly opened. The outer regulator valve is opened, and the pressure regulator valve is adjusted such that the output on the low-pressure gauge reads 5 psi. Then valve 1 is closed. The nitrogen gas is now filled in the pipelines between valves 1, 3, and 4.

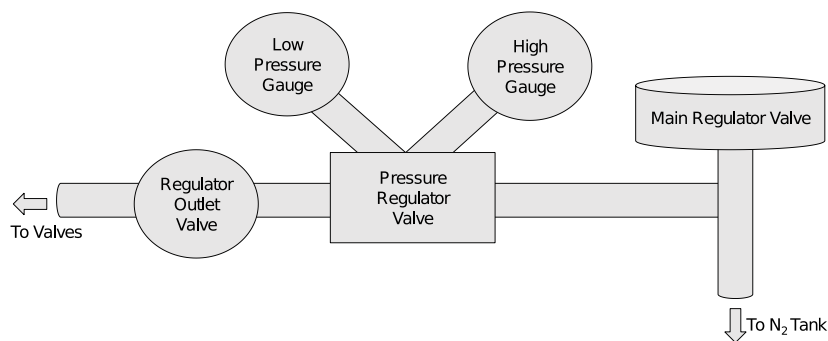


Figure 2.4. Overview of regulator and valves connected in the SCF chamber

The nitrogen gas is now used to purge the SCF chamber. It is important to purge nitrogen before using the chamber to prevent chemical degradation of the materials and to avoid combustion reactions. The latter is important to the safe operation of the SCF chamber in the presence of flammable liquids. While keeping the nitrogen gas flowing from the tank, Valve 4 is opened followed by the opening of the inlet SCF valve and then the outlet SCF valve is opened.

Nitrogen gas is now flowing through the SCF chamber. The pressure generator wheel is slowly turned clockwise until it has reached its maximum extension. It is then left in this position for 5 minutes to allow proper nitrogen purging. After 5 minutes, the outlet SCF valve is closed, followed by the closing of the inlet SCF valve to stop nitrogen purging. Valve 4 is left open and then the solvent bottle is purged with nitrogen gas. For purging the solvent bottle with nitrogen gas, the nitrogen gas should be flowing through the pipes. Also, it is important to monitor the pressure. It should not exceed 5 psi at any point in time. Valve 5 is opened followed by valve 2. Bubbles are typically observed in the solution present in the solvent bottle. It is left for 10 minutes to allow maximum deoxygenation of the solvent. After 10 minutes, valve 2 is closed, followed by the closing of valve 5 and then valve 4.

The chamber is then filled with the solvent. Valve 3 is first opened, followed by valve 5, then the SCF inlet valve, and finally the SCF outlet valve. The solvent will begin filling the SCF chamber, filling is completed when the solvent begins to flow in the cold trap. The pressure generator wheel is then opened by turning it counterclockwise to its

end to fill the solvent. The pressure generator is turned slowly to avoid any dramatic interruption in the flow of solvent. Once the chamber and the pressure generator are filled with solvent, the system must be closed. First, the SCF outlet valve is closed, followed by the SCF inlet valve, then valve 5, then valve 3, then the regulator outlet valve, the pressure regulator valve, and then finally the main regulator valve. The SCF chamber is now ready to be used at high temperatures and high pressure.

The experiment requires changing the temperature of the chamber body. This is accomplished with the help of heating cartridges settled inside the corners of the top face of the chamber. The heating cartridges are connected to the Omega benchtop Proportional Integral Derivative (PID) temperature controller (CSi32 Series with 0.04 °C temperature stability). Feedback to the PID controller is provided by sensing the chamber temperature using a thermocouple placed in mechanical contact with the chamber bottom.

A thermocouple is an electric device that can measure temperature over a wide range from -250 °C to 2300 °C. Thermocouples can show a quick response to temperature variation. They are quite easy to handle and are cost-effective temperature-sensing devices as well. It consists of two different types of metals. These metals are joined together at one end to form a junction. Heating or cooling the measuring junction of the thermocouple leads to the production of voltage. This voltage is compared with the voltage across the reference junction and is proportional to the change in temperature.

$$\Delta V = \alpha \Delta T \quad 2.1$$

Where α is known as the Seebeck coefficient.

Different types of thermocouples are used depending upon the range of temperature measurement, voltage requirement, accuracy, and atmospheric conditions, for example, reducing conditions, oxidizing conditions, inert conditions, or in a vacuum⁷⁷. The table describes the different metals used to build thermocouples for different temperature ranges.

It is important to take some precautions to increase the durability of a thermocouple such as operating the thermocouple below its design limit, avoiding very large temperature gradients along the wire, avoiding mechanical stresses and vibrations that often lead to strain distortion in the wires, using adequate external sheath to protect the wires from the

hostile atmosphere as the SCF chamber and substrate are heated at high temperatures (150 °C and 180 °C). The addition of a ground fault circuit interrupter is done between the power control unit and the wall power to ensure safety against any ground fault as shown in figure 2.5.

Table 2.1. Metals used to build thermocouples for different temperature ranges

Thermocouple type	Positive Wire	Negative Wire	Temperature Range
T	Copper	Constantan	-200 °C to 370 °C
J	Iron	Constantan	0 °C t 750 °C
E	Constantan	Chromel	-200 °C to 900 °C
K	Chromel	Alumel	-200 °C to 1250 °C
N	Nicrosil	Nisil	-200 °C to 1250 °C
S	Platinum	Platinum + 10% Rhodium	0 °C to 1450 °C

The pressure is generated from High-Pressure Equipment Co. (HiP 62-6-10) manual pressure generator which consists of a piston designed to develop and maintain the required pressure. The pressure is displayed on a LED display that is tracked by the Swagelok PTI Series transducer. As stated above, the system contains a 7500 psi pressure rupture disc fitted as a safety measure from over-pressurizing. Figure 2.6. shows in the schematic of the pressure generator with some of its key components that are connected to the SCF chamber.

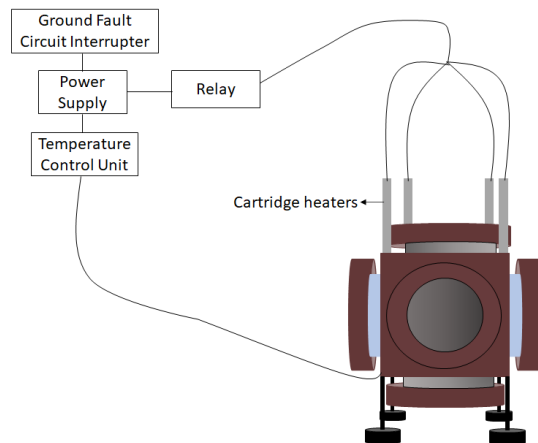


Figure 2.5. Schematic of chamber connected to power supply and temperature control unit

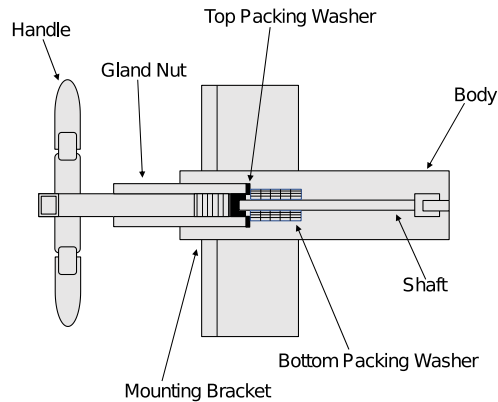


Figure 2.6. Schematic of pressure generator connected to the SCF chamber

2.2.1. Substrate Cleaning

For the film deposition, ITO-coated glass substrates are used. Indium-tin oxide (ITO) coating is used to make the transparent conductive coating on glass substrates for optoelectronic applications. These substrates are procured from Colorado Concept Coatings. The substrates are 1.5 cm² squares. The thickness of ITO coating on the glass is in the range of 40 nm to 100 nm. The average resistance of ITO coating is 20 to 60 Ω/sq. The exact ratio of indium, tin and oxygen can vary, the sheet resistance of films are typically quoted.

Proper cleaning of the substrate is an important step in device fabrication. There are dust and dirt present on substrates that need to be cleaned before use. This step is essential to achieve a successful device. Failure to do this leads to a decrease in adhesion which further leads to reduced durability and performance level of the device.

The ITO-coated glass substrates are cleaned using isopropyl alcohol. The substrates are sonicated twice for 20 minutes for removing any tightly-adhered contaminants if present. These substrates are then plasma cleaned for fifteen minutes. Plasma cleaning helps for removing surface contamination. Plasma cleaning is an effective method for critical sample preparation. It helps in preparing the substrate for further fabrication and makes it fit for any chemical bonding. The organic bonds of oil and grease contaminants present on the surface are broken by the ultraviolet light generated

in the plasma. Thereafter, the energetic oxygen present in plasma react with organic species to form water and carbon dioxide. These molecules are constantly being pumped out from the chamber resulting in a clean surface. To avoid oxidation of the substrate, Argon is passed through it.

2.2.2. Sample Preparation

After a thorough cleaning of the substrate, it is placed on the sample holder and inserted inside the supercritical fluid chamber for deposition. The temperature of the substrate is set by the thermocouple. Thermocouples are attached to the sample holder for monitoring the temperature of the substrate surface. The voltage is applied through the copper wires that are soldered to the sample holder using melted tin. The design and functioning of the sample holder are discussed in detail in this chapter.

2.3. Ultraviolet-visible Spectroscopy

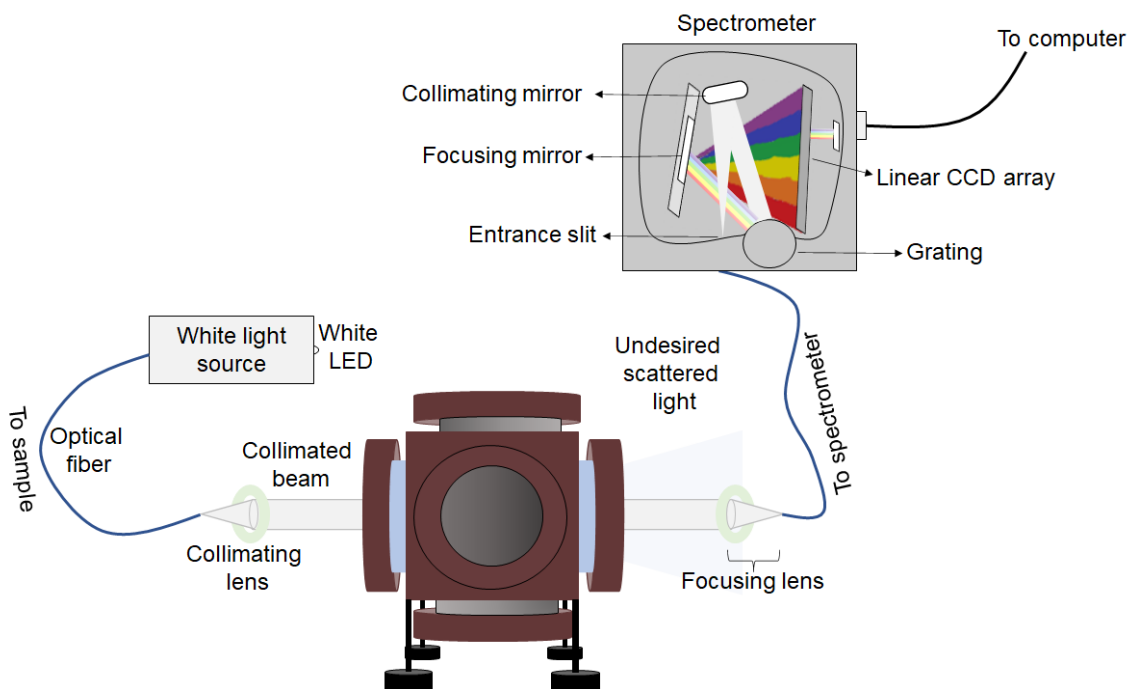


Figure 2.7. Schematic of UV-visible spectroscopy with SCF chamber setup

Ultraviolet-visible (UV-vis) spectroscopy is an extensively used spectroscopic technique in scientific research. This technique relies on the sample to be a chromophore, i.e., it should absorb light in the ultraviolet-visible region. It can evaluate the wavelength in

which the light is being absorbed or transmitted by the sample. In the electromagnetic spectrum, there are several regions present. The UV-visible spectroscopy with SCF chamber setup is shown in Figure 2.7.

The solubility properties of poly(3-hexylthiophene) (P3HT) are concluded by in-situ transmission UV-Visible spectroscopy. The UV-visible spectrometer mainly consists of the light source, monochromator, and detector. Generally, the light source used is deuterium and tungsten. Deuterium emits light in the ultraviolet region of the electromagnetic radiation spectrum whereas tungsten lamp is used for wavelengths in the visible region. The light source used is (HL-2000). It generates a broad band from 360 nm to 2400 nm. The light source and detector for UV-Visible spectroscopy are aligned in front of sapphire windows through optical fibers keeping the path length of approximately 15 cm. Ocean Optics USB4000 spectrometer is used for spectra collection. The optical fiber connects the collimating lens which produces a collimated beam of light that goes to sample through the sapphire window of the SCF chamber. The light passing through the sample reaches the spectrometer through the focusing lens. The monochromator is a diffraction grating that spreads the light into its component wavelengths. The desired wavelengths are focused by the slit. A silicon-based charge-coupled device (CCD) array more specifically, Toshiba TCD1304AP 3648-element linear silicon charged-coupled device array, bought from Ocean Optics is used for detecting light. Silicon CCDs typically can detect light between 300 nm and 1100 nm.

2.4. Film Deposition

In order to deposit films, a custom-made sample holder is used. It helps in placing the ITO-coated glass substrate inside the supercritical fluid chamber. There are two legs of polyether ether ketone (PEEK) facing two copper legs in the sample holder. There are 3 mm wide gold electrodes deposited on the sides of the substrate to allow uniform heating through the ITO by passing a current through the ITO film. The substrate is positioned in between the PEEK and copper legs ensuring that the sides of the substrate are in contact with the copper electrodes. There should be good contact with the copper electrodes and the substrate for a continuous flow of current throughout the deposition. There are four holes in the corners of the PEEK legs for screws. These screws are used to secure the substrate. After the secure positioning of the substrate, the resistance across the electrodes is noted and inserted parallel inside the chamber cell facing the ITO coating in

the upward direction. The temperature of the ITO-coated glass substrates is managed by thermocouples attached to the sample holder. Copper wires are soldered using molten tin across the sides of the sample holder. The voltage is applied to the substrate through the copper wires.

For the film deposition, the UV-Visible spectra of P3HT in solstice with 5% toluene (v/v) are studied. It is established from the spectroscopic results described in chapter 3 that the P3HT is being absorbed highest at 150 °C under the pressure of 750 psi. Therefore, the substrate pressure is set at 750 psi and the substrate temperature is set to 150 °C to get the maximum amount of P3HT deposition on it. For setting the temperature of ITO-coated glass substrates the applied voltage is in the range of 20 to 25 Volts.

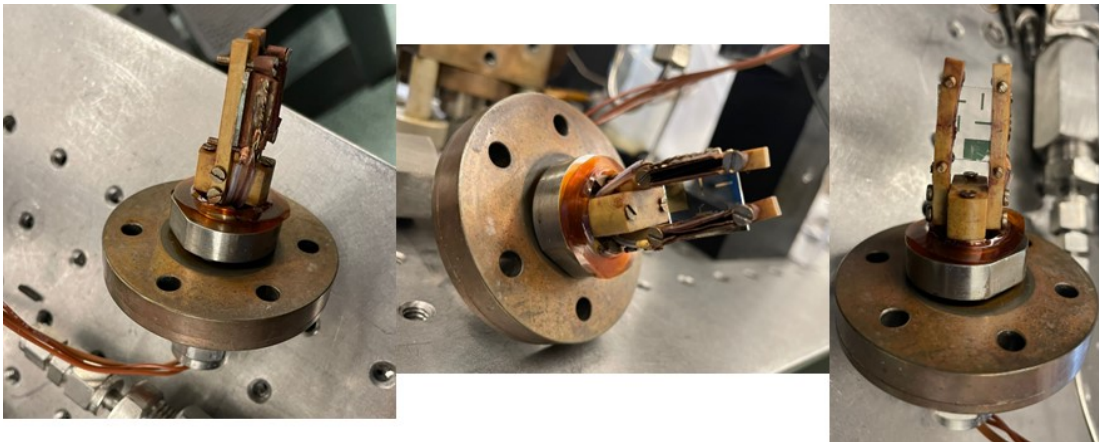


Figure 2.8. Sample holder view from the side (left), top (center), and bottom (right)

2.5. PID controller

PID stands for Proportional Integral Derivative. It is a device used for this device works regulating temperature, pressure, speed, flow, and other variables. It works on the principle of control loop feedback for variable regulation.

Temperature control of the chamber body and the ITO-coated substrate is accomplished using a PID control unit. The PID unit takes in the temperature as measured by a thermocouple and outputs a signal that drives the heating of either the cartridge heaters or the ITO glass. In practice, the system adjusts the three types of gain in order to minimize the difference between the temperature and the setpoint. The error tends to oscillate slightly from negative to positive, meaning that there is to true “zero error” state

in the system. If the gain is set correctly, these errors can be made small enough to satisfy the required accuracy.

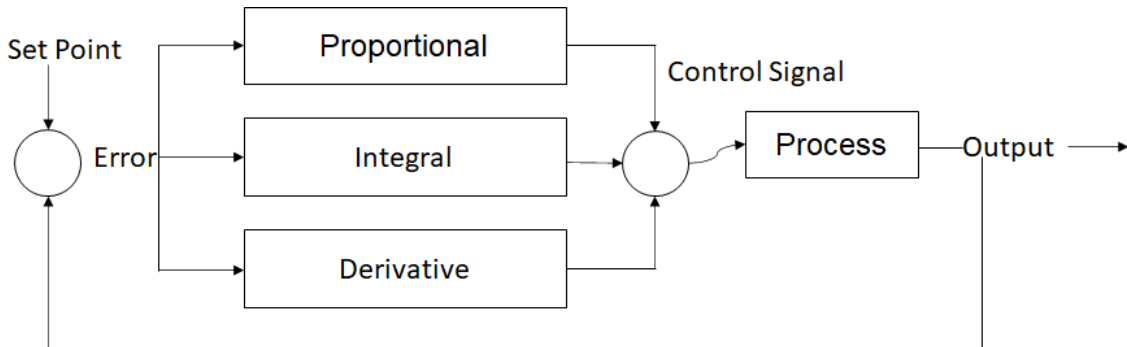


Figure 2.9. Block diagram of PID controller

The *proportional gain* helps to identify the error and thus helps in correcting the response value. It amplifies the error proportionally, providing the result to the control signal. Here, the error is the difference between the measured temperature and the setpoint. Hence, the output can be obtained by multiplying the values of error and proportional gain. The schematic below shows the flow of information through the device.

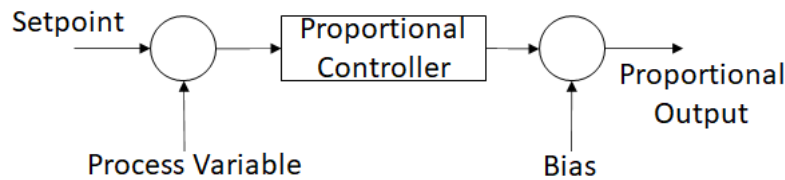


Figure 2.10. Proportional controller

The determined errors are accumulated together and are integrated with the *integral gain*. Even a small error value gives a high integral response if it persists for an extended time. Thus, the integral gain tends to force the error to oscillate between positive and negative error values, whereas the proportional gain tends only to minimize its instantaneous magnitude. Because the response involves an integral over time, the response speed tends to decrease when large values of integral gain are used. Below is a schematic illustrating the flow of information.

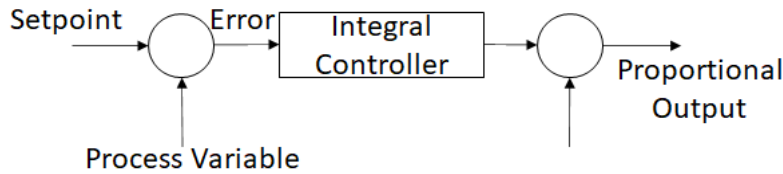


Figure 2.11. Integral controller

The *derivative gain* helps in anticipating the error values. It detects the speed of the process variable change thereby generating the corresponding value of output. The product of the rate of change of error and the derivative constant estimates the value of the output. The derivative controller improves the response speed by quickly initiating the output. This helps in predicting the rate of change of error with the derivative constant. This is important when the process variable is sluggish to respond to the control signal, a small derivative gain will help prevent a large overshoot of the setpoint. Below is a schematic illustrating the general principle.

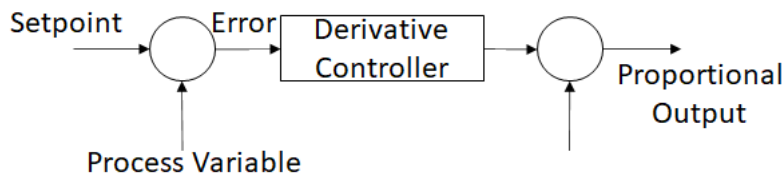


Figure 2.12. Derivative controller

2.6. Optical Microscope

An optical microscope is used to collect images of the films deposited from the supercritical fluid chamber. Optical microscopy is a technique employed to minutely view a sample through the magnification of the lens. It is often called a light microscope as it uses visible light to visualize images with the help of one or more lenses.

Depending upon the design, an optical microscope can be of many types. Its design varies from basic to complex levels propounding higher resolution. In a simple microscope, a lens is used to magnify the image whereas, in a compound microscope, a series of lenses are used to magnify sample images. The lens that is usually present at the top for looking through the sample is known as the eyepiece lens. It is often called an ocular lens. The lenses that collect and focus light to create an image are called objective lenses.

The ability of a lens to differentiate between two lines or points separated by slight angular distances to form distinguishable images is measured by its resolving power. Ernst Abbe and Carl Zeiss developed the method of resolving the power of lenses. Abbe considered the refractive index of the medium between the objective and the cover glass (n), the natural sine of one-half the angular aperture (α), and the wavelength of light (λ). He then proposed the formula for resolving power, which is given by,

$$\text{Resolving power (D)} = \frac{\lambda}{2NA} \quad 2.2$$

Where Numerical aperture $NA = n \sin \theta$ 2.3

Thus, the resolving power decreases as the angle of the light leaving the lens becomes more shallow and also decreases with increasing wavelength. For example, using light of 500 nm, a refractive index of 1, and an incident angle of 45° results in a theoretical limit of the resolving power of around 354 nm. In practice, this limit is only approached in special cases. The incoherent white light sources typically used in light microscopes are not well-collimated, and imperfections in lens geometry conspire to limit the resolution. As a counter-example, confocal microscopes use laser light sources, allowing for diffraction-limited imaging of a single point on the sample. However, recent advances using image processing of fluorescent probes have created images that beat the diffraction limit, a technique called “super-resolution imaging” that was awarded the Nobel Prize in Chemistry in 2014⁷⁸.

2.7. Probe Station

The organic field-effect transistors are measured using the probe station, a well-known tool for testing electronic devices. The device is kept on a stage and the electrical probes are placed into electrical contact on the device by manipulating them via micropositioners. In the setup used in this work, a camera is placed on top of the station to observe the position of the tips relative to the sample, allowing them to be connected to the device without damaging it. The source and gate electrodes are connected to a KEITHLEY SourceMeter (Series 2600B models). An SMU is an instrument that can source voltage or current and simultaneously measure voltage and/or current. The instrument is configured to perform voltage source-current measure operations.



Figure 2.13. Probe station (4D Labs SFU)

The setup used to measure transistors in this work contains three probes, all of which are capable of measuring the current flow into and out of the device. One probe is connected to an ammeter and is set as the drain, this channel is connected to electrical ground. Channel A and B probes are connected to the source and drain of the transistor, each is capable of sourcing voltage and measuring current simultaneously as described below. These instruments are interfaced with a computer that allows them to be controlled and the measured data to be recorded via a piece of custom-coded Labview software.

Chapter 3. Results

The physical supercritical fluid deposition is a method of thin film deposition that allows high molecular weight materials to be deposited onto curved and flexible substrates to form patterns with high spatial resolution. The preferred mode of deposition relies on a maximum in the isobaric solubility to precipitate material on to a heated substrate. This typically occurs at pressures exceeding the critical pressure of the solvent, hence the technique is termed supercritical fluid deposition. Because the technique relies on the solubility properties of the solvent-solute system, one of the most important factors in determining the optimized deposition conditions is solvent selection. Here, we demonstrate that for poly(3-hexyl thiophene) (P3HT), there are three qualitatively different types of solvents, only one of which is appropriate for physical supercritical fluid deposition on heated substrates. Over-powered solvents are ineffective for a physical supercritical fluid deposition because they lack a maximum in the isobaric solubility. Underpowered solvents are unable to dissolve the deposition material. Optimum solvents dissolve the material effectively and exhibit a maximum in isobaric solubility over the working temperature range of the deposition chamber. In addition, we demonstrate the effect of adding an over-powered solvent to an underpowered solvent and an optimum solvent. Only the mixture with an optimum solvent shows the necessary characteristics for physical supercritical fluid deposition. In sum, the work demonstrates clear guidelines for solvent selection that will allow for the deposition of a wider range of materials.

3.1. Introduction

The development of techniques for controlling matter at nanoscale dimensions has traditionally proceeded along two non-intersecting lines. The top-down approach, exemplified by photolithography, creates nanoscale structures by a subtractive process; a larger monolithic material is sectioned, and unwanted components are removed⁷⁹. The bottom-up approach, exemplified by living organisms and the techniques of macromolecular chemistry creates nanoscale structures by an additive approach; larger structures are built up via chemical bonds or strong intermolecular interactions⁸⁰.

Physical supercritical fluid deposition (p-SFD) was demonstrated as a means of connecting top-down and bottom-up approaches to controlling the structure of materials⁶².

The process relies on the existence of a maximum in the isobaric solubility of the material to be deposited. The solution is held at or near this maximum, and a substrate is heated such that material precipitates onto the substrate. Because precipitation only occurs where the substrate is heated, controlling the locus of material deposition is equivalent to controlling the local temperature on the substrate. This is conveniently accomplished by photolithographically patterning the substrate with conductive traces and employing resistive heating to control the local temperature. The material precipitates from the solution, self-assembling into the nanoscale structures dictated by intramolecular and intermolecular interactions. Thus, p-SFD harnesses both the scalability and reproducibility of photolithography as well as the complexity and subtlety afforded by solution phase self-assembly. It is important to mention that chemical supercritical fluid deposition (c-SFD)⁸² allows for the deposition of metals⁸³, inorganic films⁸⁴, in-situ polymerization reactions⁸⁵, and nanoparticle assembly⁸⁶. The terms p-SFD and c-SFD were chosen to invite the comparison between physical vapor deposition (PVD) and chemical vapor deposition (CVD).

One immediate application for p-SFD is the deposition of polymer-based circuitry⁸⁷. Organic light-emitting diodes are a successful technology that relies on the deposition of lower molecular-weight materials via PVD⁸⁸. Polymer and solution-processable molecules often form films with superior properties to their lower molecular weight counterparts⁸⁹. However, controlling the deposition of solution-processable materials with the necessary precision at scale has proven difficult. One approach is so-called orthogonal processing whereby photolithography is performed using solvents in which the semiconducting polymer is immiscible⁹⁰. Common additive deposition techniques are based on printing technologies⁹¹, each technique offers different trade-offs between scalability, ultimate resolution, and the ease of ink formulation. For example, roll-to-roll printing is perhaps the most scalable but has a lower ultimate resolution, and ink formulation to obtain the necessary high viscosity requires extensive experimentation to optimize both performance and printability⁹². Alternatively, aerosol jet printing⁹³ has the highest resolution and can print solutions with viscosities similar to those frequently encountered with spin-coating. However, the use of a print head makes large-area printing at scale a difficult proposition. Finer linewidths can be achieved with p-SFD⁸³ than aerosol jet printing¹⁰². The fact that material deposition occurs in a single step and the technique does not require a direct line-

of-sight between the material source and the substrate also presents a compelling case for its scalability.

We hypothesize that any soluble material which possesses adequate thermal stability can be deposited via p-SFD. However, choosing the correct solvent for p-SFD is not trivial. The resistive heating version of p-SFD, while technologically the most straightforward relies on the existence of a continuously varying, isobaric saturation solubility with a maximum with respect to temperature to allow for controlled material self-assembly during the deposition process⁸³. This set of conditions most often occurs above the critical pressure of the solvent. In theory, this could occur above or below the critical temperature of the solvent. This makes the strict distinction between subcritical or supercritical conditions not particularly meaningful in this context. As opposed to the Widom line, which differentiates regimes of SCF behavior at higher temperatures¹⁰³ the line between incompressible liquid and supercritical fluid typically defaults to the critical temperature¹⁰⁴, a point in the phase diagram rather than a well-defined phase boundary at all pressures. As such, we default to the terminology of supercritical fluid, although the terminology is not vital in this context. More importantly, we require that the temperature of the saturation solubility maximum occur below the decomposition temperature of the material and within the range of experimentally obtainable temperatures.

Previous studies have demonstrated the presence of an isobaric saturation solubility maximum with respect to temperature using pentane as the solvent and both isotactic polypropylene and a bithiophene-based semiconducting polymer commonly referred to as PBTTT^{62,83,84,85}. Both solutions exhibit this maximum at approximately 140 °C. Given the structural differences between the aliphatic and pi-conjugated polymers, it would be tempting to infer that this temperature is a property of the solvent and should be observed for a broad range of materials. However, this inference is incorrect, as will be shown here. In addition, the flammability of pentane makes the discovery of more inert solvents amenable to p-SFD an important step toward its broader and safer application.

Here, we report the saturation solubility of poly(3-hexylthiophene) P3HT in a variety of solvents and solvent mixtures at supercritical pressures (Figure. 3.1.b). We find that in pentane, P3HT does not exhibit a maximum in the isobaric saturation solubility. We, therefore, describe pentane as an over-powered solvent for P3HT in the context of p-SFD. We also studied the solubility of P3HT in novac (Figure. 3.1.b). We find that P3HT

exhibits very little solubility in this material and describe novac as an under-powered solvent for P3HT. Mixing novac with pentane or toluene does not provide a solvent mixture amenable to p-SFD. Instead, P3HT exhibits behavior typical of a solvent/non-solvent mixture, creating P3HT aggregates in solution. Studies of the saturation solubility of P3HT in solstice (Figure 3.1.b) show low but measurable solvation. Importantly, the isobaric saturation solubility displays a maximum with respect to temperature. Adding a small amount of toluene to solstice increases the solubility dramatically, while still displaying a solubility maximum at an accessible temperature.

3.2. Experimental

We have constructed a custom pressure cell from a block of beryllium copper (Figure. 3.1). The instrument has six ports to maximize the flexibility of experiments that can be performed with it. The configuration used for the experiments described here places the chamber inlet at the bottom where the solvent can be introduced via an external manifold. The external manifold also allows the solvents to be deoxygenated by passing a stream of nitrogen through the solvent for at least 30 minutes prior to introducing the solvent into the main body of the pressure cell. This deoxygenation step and the complete filling of the cell is an important safety measure when using flammable solvents like pentane. A manual pressure generator is connected to the inlet as is a pressure transducer. The chamber outlet is located at the top of the vessel such that the entire chamber volume can be filled with solvent, thus excluding all but trace amounts of oxygen. As an additional safety measure, the entire pressurized system was surrounded with a Lexan enclosure which was under constant ventilation to prevent the buildup of solvent vapors.

Heating is accomplished by four cartridge heaters, placed into small holes on the top of the vessel. The cartridge heaters are wired in parallel and connected to a DC power supply via a relay with a ground fault circuit interrupter. The relay is controlled by a temperature control unit, which reads the cell temperature using a type K thermocouple secured to the bottom of the cell. During all measurements, the temperature and pressure were allowed to equilibrate for 15 minutes prior to measurements.

The cell has two sapphire windows placed opposite each other to enable in-situ UV-Vis measurements of the cell contents. Spectroscopic measurements were collected

with an Ocean Optics USB 4000 spectrometer which covers a range of 200–1100 nm using a Toshiba TCD1304AP (3648-element linear silicon CCD array) detector. The light source was a halogen bulb (HL-2000, ocean optics) emitting over a wavelength range of 360 nm - 1100 nm. The reference spectra used for each absorbance measurement were collected at room temperature. A reference spectrum was collected at each pressure, to avoid artifacts due to the pressure dependence of the refractive index of the solution.

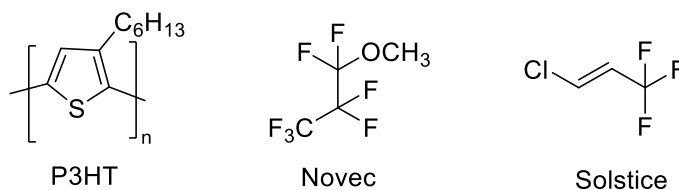


Figure 3.1. Chemical structures of compounds used in this study: P3HT, Novec and Solstice

Regioregular P3HT (Mw =58 kg/mol) was obtained from Brilliant Matters and used as received. It was placed into a glass crucible that was capped with glass wool and a copper mesh to prevent undissolved material from dispersing into the solution. Novec (Tc=165 °C, Pc=360 psi)¹⁰⁵, n-pentane (Tc=197 °C, Pc=489 psi), and toluene (Tc=319 °C, Pc=599 psi) were obtained from Millipore-Sigma and used as received. Solstice (Tc=166 °C, Pc=547 psi)¹⁰⁶ was obtained from Honeywell and used as received. Because of the low boiling point of n-pentane, novec, and solstice, they were held in a glass bottle that was immersed in dry ice while being purged with nitrogen (99% purity, Praxair).

The P3HT films are deposited onto ITO-coated glass substrates. The temperature of the cell wall is held at the temperature of solubility maximum and resistively heating substrate at a temperature of decreased solubility. Since the substrate is present at a temperature of lower solubility, the material precipitates out of the solution to form a film. also, describe the microscope you used to collect the images. Optical microscope images of P3HT films grown on heated ITO-coated glass substrates are taken using Zeiss Axio Observer Microscope. The exposure and saturation in these optical images are adjusted to study films. The image resolution was 50 μm , which provides visual confirmation of P3HT films and their microscale morphology.

3.3. Results and discussion

3.3.1. Solubility study of P3HT in pentane

In order to measure the solubility properties of P3HT in a variety of solvents, in-situ UV-Vis spectroscopy was performed on the pressure cell through sapphire windows placed on opposite sides of the cell. Figure. 3.2.a shows a representative spectrum of P3HT in n-pentane collected at 1500 psi (103 bar). The spectrum shows a peak typical of well-dissolved P3HT that increases monotonically with pressure. As the absorbance approaches 3, the spectrum becomes noisy as a result of very little light reaching the detector. As the temperature increases, the absorbance increases, indicating that the amount of dissolved material is increasing.

Figure. 3.2.b shows the value of the absorbance at 490 nm as a function of temperature for several different pressures. The absorbance increases monotonically at lower temperatures, reaching a plateau at the highest temperatures. The same data is plotted in Figure. 3.2.c but with respect to pressure at several temperatures. At the lowest temperatures, the absorbance increases with pressure while at the highest temperatures, the response with respect to pressure is relatively flat. The integrated absorbance will not be affected by changes to the line shape associated with temperature and pressure changes as dictated by quantum mechanics sum rules.

In a typical solution, the amount of dissolved material increases with respect to temperature¹⁰⁷. This is a natural result of the entropy of solvation, an effect we observe at lower temperatures. At higher temperatures, the contribution of the solvent to the entropy of solvation becomes more important^{83,108,109}. Dissolution requires the formation of a solvent shell around the polymer¹¹⁰ and as such, the process of solvent shell formation has a negative entropy. The molecules surrounding the polymer are no longer free to move about the entire volume of the solvent. The higher density of the solvent shell around the polymer is confirmed by the pressure dependence of the solubility, which exhibits an increase with respect to pressure.

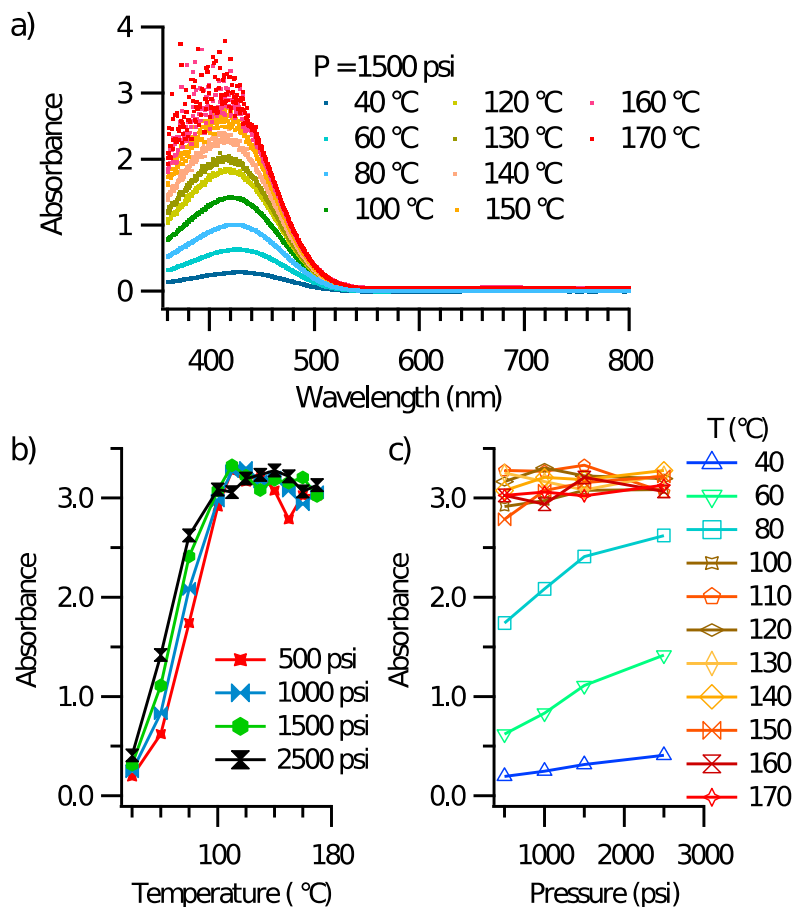


Figure 3.2. Solubility data for P3HT in pentane. (a) UV-Vis of P3HT in n-pentane collected at 1500 psi (b) Absorbance at 490 nm for several pressures as a function of temperature (c) Absorbance at 490 nm for several temperatures as a function of pressure

Hence, the volume change of solvation is negative, leading to a larger free energy of solvation with increasing pressure. This effect is typically unimportant in a regular solution, where the fluid is approximately incompressible. In fact, the incompressibility of the solvent is a key assumption in the Flory-Huggins theory of polymer solutions. As the temperature of the solvent approaches the critical temperature, the density of the medium decreases, and the compressibility of the solvent increases¹⁰⁴, making the effect of solvent entropy during solvation a more important consideration. This is the reason that the solubility plateaus at higher temperatures, and in general will lead to an eventual decrease in the saturation solubility of the polymer at sufficiently high temperatures. However, our instrument is not able to access temperatures high enough to observe the decrease.

Additionally, the thermal stability of P3HT is finite, with polymer decomposition typically being observed at 420 °C. These observations make pentane an unsuitable solvent for p-SFD with our instrument, which requires a maximum in the isobaric saturation solubility with respect to temperature. We, therefore, classify pentane as an over-powered solvent for P3HT.

3.3.2. Solubility study of P3HT in solutions containing novoc

In order to find a less powerful solvent for P3HT and move towards less flammable materials, we investigated novoc, a commercially available flame retardant compound¹¹¹. The results of in-situ UV-Vis spectroscopic measurements are shown in Figure. 3.3.a at P=1000 psi (69 bar) at T=150 °C for several solutions containing novoc. In pure novoc, P3HT is practically insoluble at all temperatures as shown in Figure. 3.3.b and 3.3.c. Increasing the pressure did not improve the ability of novoc to dissolve P3HT. We, therefore, classify novoc as an under-powered solvent for P3HT. It is unsuitable for use in p-SFD because it is not able to dissolve the deposition material.

To improve the solvating power of novoc, toluene was added. Toluene is known as a good solvent for P3HT, solutions of appreciable concentration can be created at room temperature and atmospheric pressure. It is worth mentioning in passing that we avoid terming solvents as good or bad in this context. The word “good” implies a desired outcome and as such, the terminology is inherently subjective. Instead, we describe solvents with high saturation solubilities as powerful solvents for a particular solute.

At low concentrations of toluene (5% and 20% v/v; atmospheric pressure), the solubility of P3HT in our pressure cell was not demonstrably increased, or at the very least, does change with respect to temperature as shown in Figure. 3.3.a and 3.3.b. Recall that the filled cell at room temperature is used as the background in the calculation of absorbance, meaning that we are only able to detect changes to the saturation solubility rather than their magnitude relative to the solvent alone. As the concentration of toluene is increased to 50%, the saturation solubility of P3HT increases dramatically, as demonstrated by the increasing absorbance at 490 nm in Figure. 3.3.b. However, Figure. 3.3.a shows a negative-going absorbance feature between 510 nm and 650 nm. Since the background used in calculating absorbance is the filled cell at room temperature, a

negative-going feature indicates the presence of a species at room temperature that was removed upon heating the cell.

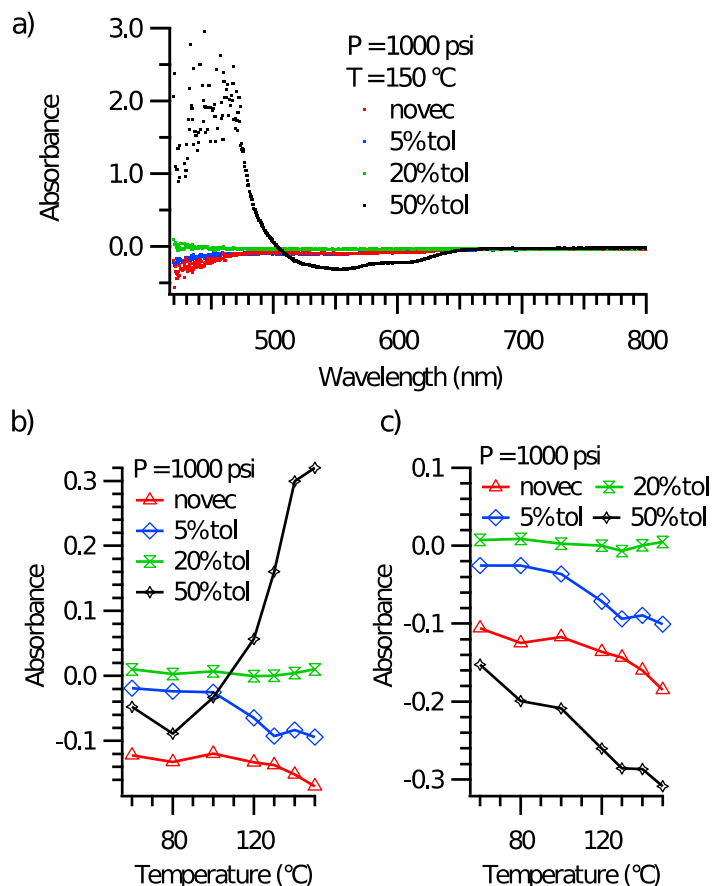


Figure 3.3. Solubility data for P3HT in novect. (a) UV-Vis of P3HT in several solutions containing novect collected at 1000 psi and 150 °C (b) Absorbance as a function of temperature at 1000 psi and 490 nm (c) Absorbance as a function of temperature at 1000 psi and 550 nm

The negative-going feature has the vibronic progression characteristic of aggregated P3HT^{112,113}. We thus conclude that at high toluene concentrations, P3HT is dissolved as collapsed aggregates at room temperature. Figure. 3.3.c shows the absorbance at 550 nm as a function of temperature. With increasing temperature, the negative-going feature becomes more negative, indicating that the aggregates are undone, and are dispersed as well-dissolved material. Some evidence of this is also present with lower concentrations of toluene as shown in Figure. 3.3.c. The formation of P3HT aggregates in mixtures of weak and powerful solvents is well-documented in systems like chloroform/ ethyl acetate¹¹⁴ and is consistent with the situation we observe in

solutions of toluene/novec. Negative going feature is strongly red shifted as compared to well dissolved P3HT. Thus, novec is not made useful as a solvent for p-SFD through the addition of a powerful solvent like toluene, with similar effects being observed with pentane/novec mixtures as shown in Figure 3.4. Stated more generally, the combination of weak and powerful solvents does not make an optimum solvent but rather exhibits an entirely different behavior that remains unhelpful for p-SFD.

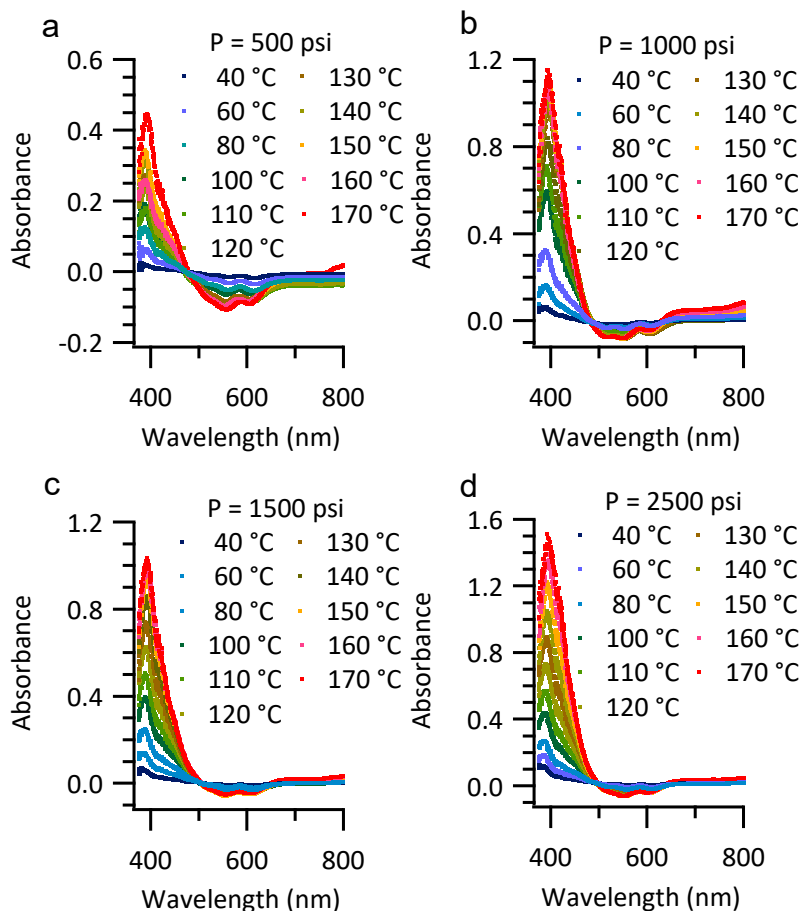


Figure 3.4. Solubility data for P3HT in novac and pentane. (a) UV-Vis of P3HT in novac and pentane collected at 500 psi (b) at 1000 psi (c) 1500 psi (d) at 2500 psi

3.3.3. Solubility study of P3HT in solutions containing solstice

Solstice is a non-flammable, although not flame-retardant compound often used for cleaning¹¹⁵. The conjugated bonds in this molecule suggest that it might be a more effective solvent for P3HT, a pi-conjugated polymer. Figure. 3.5 shows the results of an in-situ UV-Vis experiment of our cell containing solstice and P3HT. The absorbance is

relatively low, but increases with respect to temperature, reaching a maximum at 160 °C and decreasing as the temperature is further increased.

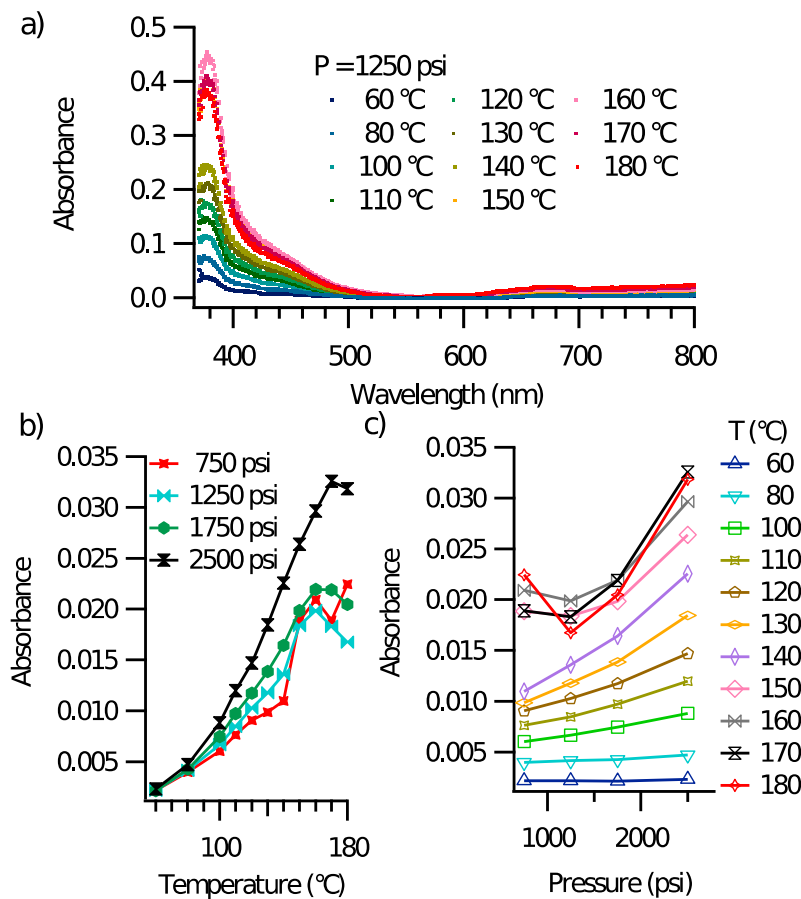


Figure 3.5. Solubility data for P3HT in solstice. (a) UV-Vis of P3HT in solstice collected at 1250 psi (b) Absorbance at 490 nm for several pressures (c) Absorbance at several temperatures as a function of pressure

The behavior is more easily visualized in Figure. 3.5.b which displays the absorbance at 475 nm plotted as a function of temperature for several different pressures. The isobaric saturation solubility in this system reaches a maximum and decreases at the highest temperatures we studied. The same data is plotted in Figure. 3.5.c as absorbance vs pressure for several different temperatures. The saturation solubility increases with pressure, indicating a negative ΔV of solvation. The existence of a maximum in the isobaric saturation solubility with respect to temperature demonstrates that solstice is an optimal solvent for P3HT in the context of p-SFD. It is neither too powerful nor too weak, displaying the necessary non-monotonic behavior as the temperature increases.

However, the in-situ UV-Vis measurements in Figure. 3.5.a does not display spectra typical of well-dissolved P3HT. Instead, they are significantly blue-shifted which we interpret as the spectrum of low molecular weight fragments and other chemically defective components of P3HT. Despite displaying optimum behavior for p-SFD, solstice does not dissolve the high molecular weight material that is preferred for optoelectronic applications.

To improve the quality of the dissolved material in solstice, toluene was added at a (room temperature, atmospheric pressure) volume ratio of 5%. A representative in-situ UV-Vis absorption spectrum of the cell contents is shown in Figure. 3.6.a. The strongly blue-shifted spectral lineshape is observed at the lowest temperatures but displays significant absorption at longer wavelengths at higher temperatures. We interpret this to indicate that higher molecular weight material is being dissolved at higher temperatures. Figure. 3.6.b displays the absorbance at 475 nm plotted as a function of temperature for several different pressures. A maximum in the absorbance is clearly observed, which we interpret as demonstrating a maximum in the isobaric saturation solubility with respect to temperature, optimum solvent behavior for p-SFD. The UV-Vis absorption feature blue-shifts as the peak in solubility is passed, demonstrating that the high molecular weight material dissolved before the peak is the first to precipitate from the solution once the peak is passed. This “last in-first out” behavior and the corresponding non-monotonic shift of absorbance features associated with the dissolved material were also observed in another pi-conjugated polymer⁶². Taken in sum, the mixture of toluene in solstice exhibits desirable properties as a solvent system for the p-SFD of P3HT.

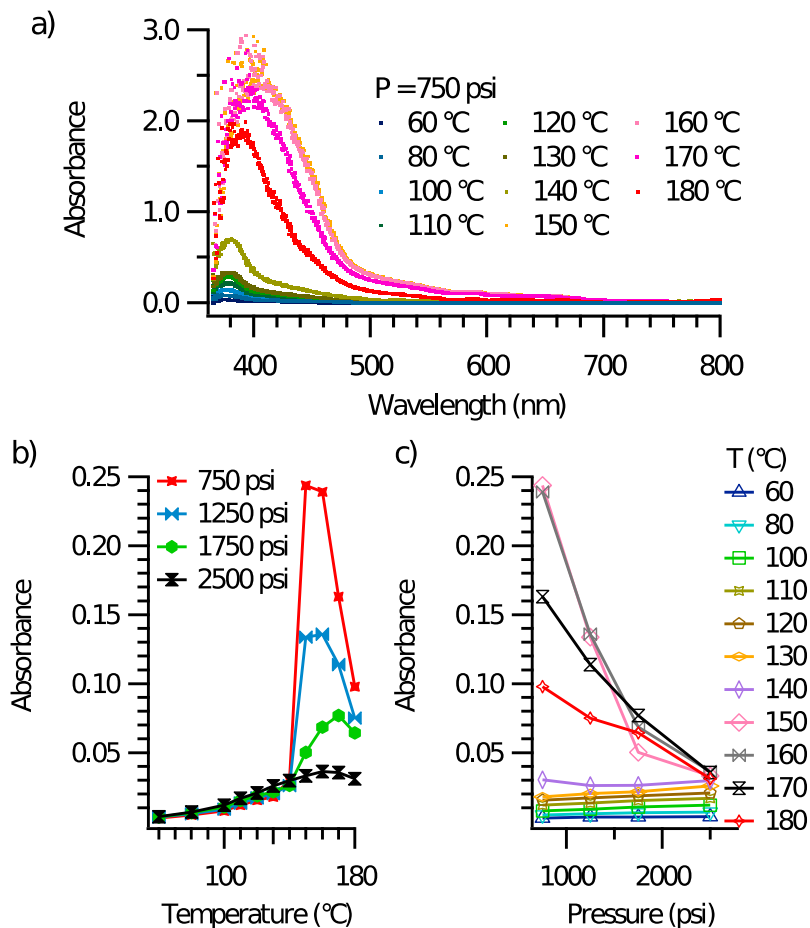


Figure 3.6. Solubility data of P3HT in solstice/toluene mixtures. (a) UV-Vis of P3HT in solstice/toluene (5%) collected at 750 psi (b) Absorbance for several pressures as a function of temperature (c) Absorbance at several temperatures as a function of pressure

The absorbance as a function of pressure for several different temperatures is displayed in Figure. 3.6.c. At low temperatures, the absorbance is independent of pressure, indicating that the amount of dissolved material is independent of pressure, implying a smaller ΔV of solvation. At higher temperatures, the amount of dissolved material drops sharply with pressure, implying a positive ΔV of solvation. We hypothesize that the solvent shell around P3HT is primarily composed of toluene and as such, the ΔV of solvation describes the change in volume associated with the solstice/toluene mixture. If removing toluene from this mixture increases the solvent volume, this implies that the ΔV of solvation of toluene in solstice is negative.

3.3.4. Film growth of P3HT using p-SFD deposition technique

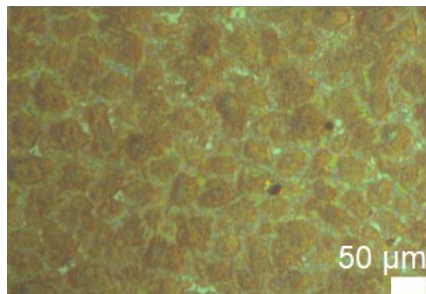


Figure 3.7. Optical microscope image taken at a resolution of 50 μm showing a thin film of P3HT deposited on a resistively heated ITO glass substrate from a solstice/toluene (5%) solution

Figure. 3.7 contains an optical microscope image of P3HT on a resistively heated ITO glass substrate that was formed using p-SFD. In this experiment, the pressure was held at 750 psi, the cell wall was held at 150 °C and the substrate was heated to 180 °C. The presence of P3HT on the substrate demonstrates the suitability of the solstice/toluene mixture as a solvent system for p-SFD of P3HT. However, the morphology of the resulting film is that of islands rather than a continuous film. We interpret this as evidence of high surface energy between P3HT and ITO, demonstrating that further optimization is required before films of suitable quality for optoelectronic applications can be formed.

3.4. Summary

In summary, solvents and solvent systems capable of use for the p-SFD of P3HT were investigated. It was found that pentane is too powerful of a solvent, exhibiting an increase in the saturation solubility of P3HT as a function of temperature, with a plateau instead of a decrease at the highest temperatures. Novec was investigated as a potential solvent and was found to be incapable of dissolving P3HT. A 50% mixture of novec and toluene was able to dissolve P3HT, however, the solution was found to contain aggregates and did not exhibit a decrease in the isobaric saturation solubility with respect to temperature at the temperatures measured here. It is therefore unsuitable for use in p-SFD. Solstice contains an allyl group and was therefore hypothesized to be a slightly more powerful solvent for P3HT than novec, but less powerful than pentane. The saturation solubility of P3HT in solstice was modest, validating this hypothesis. In addition, the temperature-dependent saturation solubility shows a maximum at approximately 160 °C,

demonstrating its utility for p-SFD. However, the UV-Vis spectra collected of the solution suggested that only low molecular weight and/or chemically defective fragments of P3HT were being dissolved, leading us to examine the effect of adding a small amount of toluene to the solstice solution. The UV-Vis spectrum of this solution indicates that higher quality material was dissolved at higher temperatures, near the peak of the solubility with respect to temperature. As a result, we used the 5% toluene/solstice solution to deposit P3HT onto an ITO-coated glass slide using p-SFD. The resulting films were not of especially high quality, demonstrating that the P3HT-substrate interaction must also be optimized. The work illustrates a general *modus-operandi* for choosing solvents in p-SFD. Namely, solvents can be found to be either too powerful or too weak for use in p-SFD. Solvent mixtures do not change this underlying behavior. Instead, chemical intuition can be used to select an optimum solvent, and a small amount of solvent additive can be introduced to modify the amount and type of material that is dissolved.

Chapter 4. Conclusions and Future Directions

In this thesis, the focus was to allow thin film deposition of high molecular weight materials using the physical supercritical fluid deposition technique. It is a solution-based technique with no requirement for in-situ chemical reactions. The deposition method relies on a maximum in the isobaric solubility to precipitate material onto a heated substrate. This typically occurs at pressures above the critical pressure of the solvent hence the technique is termed supercritical fluid deposition. In order to do this, there is a custom-made supercritical fluid chamber in our lab which is made up of copper beryllium. The chamber exterior is in the shape of a cube with an external volume of 30 mL. The chamber has two sapphire windows on opposite sides to allow the collection of UV-visible spectra. All the material solubility experiments are done using the SCF chamber. Each component in it can withstand at least 200 °C of temperature and 7000 psi of pressure. The semiconducting polymer studied is poly(3-hexylthiophene) commonly known as P3HT. The solubility behavior of P3HT is studied in different solvent systems. We have categorized the studied solvent systems into three different types. One of them being appropriate for physical supercritical fluid deposition. In pentane, P3HT does not exhibit a maximum in isobaric saturation solubility. Therefore, we have described pentane as over-powered solvent for P3HT in the context of p-SFD. In novoc, P3HT exhibits very little solubility. Therefore, we have described novoc as under-powered solvent for P3HT in the context of p-SFD. Mixing novoc with pentane or toluene does not provide a solvent mixture amenable to p-SFD. Instead, P3HT creates aggregates in the solution. In solstice, P3HT exhibits a maximum in isobaric saturation solubility but measurable solvation. Adding a small amount (5% v/v) of toluene to solstice increases the solubility dramatically, while still displaying a solubility maximum at an accessible temperature.

After getting an appropriate solvent system for P3HT p-SFD, we grew films of P3HT. Interpretation of UV-visible spectra shows that the maximum precipitation of P3HT on to heated substrate can be achieved when the chamber wall temperature is set at 150 °C and the pressure is set to 750 psi while keeping the temperature of the substrate at 180 °C. All the depositions are done under these conditions. We have used an ITO-coated glass substrate for depositing films of P3HT in solstice and 5% toluene (v/v). Some of the optical images of P3HT films deposited from p-SFD deposition are shown in figure 4.2.

Table 4.1. Summary behavior of P3HT in different solvent systems in p-SFD

Solvent system	Solubility behavior of P3HT
Pentane	Monotonic increase with temperature
Novec	Low solubility
Novec + Toluene [(5%), (20%)]	Low solubility
Novec + Toluene (50%)	Aggregate formation
Novec + Pentane (50%)	Aggregate formation
Solstice	Non-monotonic increase with temperature
Solstice + Toluene (5%)	Non-monotonic increase with temperature with higher solubility

The electronic properties of P3HT-based films using p-SFD can be investigated. First, P3HT-based organic field-effect transistors are prepared by spin coating the P3HT, the results of which are shown in Figure 4.1. This is a preliminary step to understand the OFET preparation of P3HT-based films using p-SFD. We prepared bottom gate top contact OFET devices of P3HT. The electrodes used in OFET are gold of 70 nm thickness. The dielectric is made by spin-coating poly(methacrylate) (PMMA) of molecular weight nearing 120,000 by GPC. PMMA in butyl acetate (80mg/mL) solution was spin-coated on ITO-coated glass substrate at a spin speed of 1500 rpm for 60 seconds to form a dielectric layer. The deposition condition in p-SFD is quite harsh. The temperature goes up to 180 °C and the pressure to 750 psi. Therefore, it is important to avoid PMMA dissolution in the solvent under extreme conditions. To do so, films are crosslinked at 230 °C for 30 minutes¹¹⁶. Crosslinking was demonstrated by the insoluble nature of the resulting films. The P3HT solution is prepared in dichlorobenzene (10mg/mL) and is spin-coated at 2000 rpm for 60 seconds to form the semiconducting layer on OFET. The thickness of the films can be measured using ellipsometry, atomic force microscopy, or profilometry. The thickness of these films were not quantified. The device was measured using a probe station. The output and transfer curves are shown in Figure 4.1.

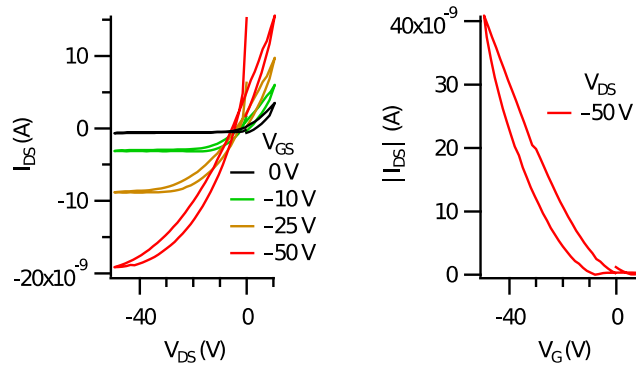


Figure 4.1. Output curve (left) and Transfer curve (right) for P3HT based top contact bottom gate organic field-effect transistor

The devices made from spin coating the P3HT layers look promising as they show transistor behavior as shown in figure 4.1(right). These OFETs are in top contact bottom gate configuration as pictured in figure 1.19. The left figure is the output curve plot of the drain current as a function of drain voltage for different gate voltages. The right figure in figure 4.1 is the transfer curve plot of the drain current as a function of gate voltage for a given source-drain voltage. The current obtained is low. Therefore, further optimization of these devices is required.

Optical images of some of the P3HT films grown for four hours using p-SFD are shown in the Figure. 4.2. The width of the white lines at the bottom right of each image is meant to indicate the length of the scale bar. Figure 4.2(a) shows an optical image of the direct deposition of P3HT onto the substrate, (b) shows 20 minutes of plasma cleaning of the substrate was done before P3HT deposition, (c) shows octadecyltrichlorosilane (OTS) treatment was done after plasma cleaning of the substrate, then a layer of PMMA was crosslinked on to it before depositing P3HT. The ITO-coated glass substrates were kept in 5 mM OTS prepared in bicyclohexyl for 6 hours. They were then rinsed with toluene and then annealed at 180 °C for an hour. This figure shows how the optimization was done in growing films of P3HT to obtain better film uniformity. However, further optimization is required to achieve higher mobility in organic field-effect transistors.



Figure 4.2. Optical images showing optimization of uniformity in P3HT films by p-SFD deposited on ITO-coated glass

References

- (1) He, Z.; Zhang, Z.; Bi, S.; Chen, J.; Li, D. Conjugated Polymer Controlled Morphology and Charge Transport of Small-Molecule Organic Semiconductors. *Sci. Rep.* **2020**, *10* (1), 1–9.
- (2) Holliday, S.; Donaghey, J. E.; McCulloch, I. Advances in Charge Carrier Mobilities of Semiconducting Polymers Used in Organic Transistors. *Chem. Mater.* **2014**, *26* (1), 647–663.
- (3) Osaka, I.; Takimiya, K. Backbone Orientation in Semiconducting Polymers. *Polymer (Guildf)*. **2015**, *59*, A1–A15.
- (4) Lei, T.; Guan, M.; Liu, J.; Lin, H.-C.; Pfattner, R.; Shaw, L.; McGuire, A. F.; Huang, T.-C.; Shao, L.; Cheng, K.-T.; Tok, J. B.-H.; Bao, Z. Biocompatible and Totally Disintegrable Semiconducting Polymer for Ultrathin and Ultralightweight Transient Electronics. *Proc. Natl. Acad. Sci.* **2017**, *114* (20), 5107–5112.
- (5) Wang, H.; Bao, Z. Conjugated Polymer Sorting of Semiconducting Carbon Nanotubes and Their Electronic Applications. *Nano Today* **2015**, *10* (6), 737–758.
- (6) Liu, C.; Sirringhaus, H. Electron Transport along Semiconducting Polymer Heterojunctions. *Org. Electron.* **2010**, *11* (4), 558–563.
- (7) Luo, C.; Kyaw, A. K. K.; Perez, L. A.; Patel, S.; Wang, M.; Grimm, B.; Bazan, G. C.; Kramer, E. J.; Heeger, A. J. General Strategy for Self-Assembly of Highly Oriented Nanocrystalline Semiconducting Polymers with High Mobility. *Nano Lett.* **2014**, *14* (5), 2764–2771.
- (8) Asawapirom, U.; Bulut, F.; Farrell, T.; Gadermaier, C.; Gamerith, S.; Güntner, R.; Kietzke, T.; Patil, S.; Piok, T.; Montenegro, R.; Stiller, B.; Tiersch, B.; Landfester, K.; List, E. J. W.; Neher, D.; Sotomayor Torres, C.; Scherf, U. Materials for Polymer Electronics Applications – Semiconducting Polymer Thin Films and Nanoparticles. *Macromol. Symp.* **2004**, *212* (1), 83–92.
- (9) Nielsen, C. B.; Giovannitti, A.; Sbircea, D.-T.; Bandiello, E.; Niazi, M. R.; Hanifi, D. A.; Sessolo, M.; Amassian, A.; Malliaras, G. G.; Rivnay, J.; McCulloch, I. Molecular Design of Semiconducting Polymers for High-Performance Organic Electrochemical Transistors. *J. Am. Chem. Soc.* **2016**, *138* (32), 10252–10259.
- (10) Yousefi, N.; Maala, J. J.; Louie, M.; Storback, J.; Kaake, L. G. Physical Supercritical Fluid Deposition: Patterning Solution Processable Materials on Curved and Flexible Surfaces. *ACS Appl. Mater. Interfaces* **2020**, *12* (15), 17949–17956

- (11) Knox, D. E. Solubilities in Supercritical Fluids. *Pure Appl. Chem.* **2005**, *77* (3), 513–530.
- (12) Deutsch, D. Quantum Theory of Probability and Decisions. *Proc. R. Soc. A Math. Phys. Eng. Sci.* **1999**, *455* (1988), 3129–3137.
- (13) Edmiston, C.; Ruedenberg, K. Localized Atomic and Molecular Orbitals. *Rev. Mod. Phys.* **1963**, *35* (3), 457–464.
- (14) Gutzwiller, M. C.; José, J. V. Chaos in Classical and Quantum Mechanics. *Phys. Today* **1991**, *44* (11), 94–96.
- (15) Takahashi, M. Looking at Molecular Orbitals in Three-Dimensional Form: From Dream to Reality. *Bull. Chem. Soc. Jpn.* **2009**, *82* (7), 751–777.
- (16) Olsen, J.; Godefroid, M. R.; Jönsson, P.; Malmqvist, P. Å.; Fischer, C. F. Transition Probability Calculations for Atoms Using Nonorthogonal Orbitals. *Phys. Rev. E* **1995**, *52* (4), 4499–4508.
- (17) Nguyen, K. T.; Blum, L. C.; van Deursen, R.; Reymond, J.-L. Classification of Organic Molecules by Molecular Quantum Numbers. *ChemMedChem* **2009**, *4* (11), 1803–1805.
- (18) Simenel, C.; Umar, A. S.; Godbey, K.; Dasgupta, M.; Hinde, D. J. How the Pauli Exclusion Principle Affects Fusion of Atomic Nuclei. *Phys. Rev. C* **2017**, *95* (3), 31601.
- (19) Mulliken, R. S. Spectroscopy, Molecular Orbitals, and Chemical Bonding. *Science* (80-.). **1967**, *157* (3784), 13–24.
- (20) Fujimoto, H.; Koga, N.; Fukui, K. A Coupled Fragment Molecular Orbital Method for Interacting Systems. *J. Am. Chem. Soc.* **1981**, *103* (25), 7452–7457.
- (21) Beaujuge, P. M.; Amb, C. M.; Reynolds, J. R. Spectral Engineering in π -Conjugated Polymers with Intramolecular Donor–Acceptor Interactions. *Acc. Chem. Res.* **2010**, *43* (11), 1396–1407.
- (22) Zhang, S.; Ye, L.; Wang, Q.; Li, Z.; Guo, X.; Huo, L.; Fan, H.; Hou, J. Enhanced Photovoltaic Performance of Diketopyrrolopyrrole (DPP)-Based Polymers with Extended π Conjugation. *J. Phys. Chem. C* **2013**, *117* (19), 9550–9557.
- (23) Griffith, M. G.; Goodman, L. Sigma and Pi Electronic Reorganization in Acetylene. *J. Chem. Phys.* **1967**, *47* (11), 4494–4504.
- (24) Yassar, A.; Roncali, J.; Garnier, F. Conductivity and Conjugation Length in Poly(3-Methylthiophene) Thin Films. *Macromolecules* **1989**, *22* (2), 804–809.

- (25) Asada, K.; Kobayashi, T.; Naito, H. Control of Effective Conjugation Length in Polyfluorene Thin Films. *Japanese J. Appl. Physics, Part 2 Lett.* **2006**, *45* (8–11), 6–9.
- (26) Ferchichi, K.; Bourguiga, R.; Lmimouni, K.; Pecqueur, S. Concentration-Control in All-Solution Processed Semiconducting Polymer Doping and High Conductivity Performances. *Synth. Met.* **2020**, *262*, 116352.
- (27) Dörfling, B.; Sandoval, S.; Kankla, P.; Fuertes, A.; Tobias, G.; Campoy-Quiles, M. Exploring Different Doping Mechanisms in Thermoelectric Polymer/Carbon Nanotube Composites. *Synth. Met.* **2017**, *225*, 70–75.
- (28) Yoon, S. E.; Kang, Y.; Noh, S. Y.; Park, J.; Lee, S. Y.; Park, J.; Lee, D. W.; Whang, D. R.; Kim, T.; Kim, G.-H.; Seo, H.; Kim, B.-G.; Kim, J. H. High Efficiency Doping of Conjugated Polymer for Investigation of Intercorrelation of Thermoelectric Effects with Electrical and Morphological Properties. *ACS Appl. Mater. Interfaces* **2020**, *12* (1), 1151–1158.
- (29) Glauddell, A. M.; Cochran, J. E.; Patel, S. N.; Chabinyk, M. L. Impact of the Doping Method on Conductivity and Thermopower in Semiconducting Polythiophenes. *Adv. Energy Mater.* **2015**, *5* (4), 1401072.
- (30) Cho, N.; Yip, H.-L.; Davies, J. A.; Kazarinoff, P. D.; Zeigler, D. F.; Durban, M. M.; Segawa, Y.; O'Malley, K. M.; Luscombe, C. K.; Jen, A. K.-Y. In-Situ Crosslinking and n-Doping of Semiconducting Polymers and Their Application as Efficient Electron-Transporting Materials in Inverted Polymer Solar Cells. *Adv. Energy Mater.* **2011**, *1* (6), 1148–1153.
- (31) Wei, L.; Zhou, P.; Yang, Q.; Yang, Q.; Ma, M.; Chen, B.; Xiao, L. Fabrication of Bright and Small Size Semiconducting Polymer Nanoparticles for Cellular Labelling and Single Particle Tracking. *Nanoscale* **2014**, *6* (19), 11351–11358.
- (32) Shen, T.; Zhou, H.; Xin, J.; Fan, Q.; Yang, Z.; Wang, J.; Mei, T.; Wang, X.; Wang, N.; Li, J. Controllable Microstructure of Polymer-Small Molecule Blend Thin Films for High-Performance Organic Field-Effect Transistors. *Appl. Surf. Sci.* **2019**, *498*, 143822.
- (33) Afraj, S. N.; He, G.-Y.; Lin, C.-Y.; Velusamy, A.; Huang, C.-Y.; Lin, P.-S.; Vegiraju, S.; Huang, P.-Y.; Ni, J.-S.; Yau, S.-L.; Tung, S.-H.; Minari, T.; Liu, C.-L.; Chen, M.-C. Solution-Processable Multifused Thiophene Small Molecules and Conjugated Polymer Semiconducting Blend for Organic Field Effect Transistor Application. *Adv. Mater. Technol.* **2021**, *6* (3), 2001028.
- (34) Kline, R. J.; McGehee, M. D.; Kadnikova, E. N.; Liu, J.; Fréchet, J. M. J. Controlling the Field-Effect Mobility of Regioregular Polythiophene by Changing the Molecular Weight. *Adv. Mater.* **2003**, *15* (18), 1519–1522.

- (35) Jackson, N. E.; Savoie, B. M.; Kohlstedt, K. L.; Olvera de la Cruz, M.; Schatz, G. C.; Chen, L. X.; Ratner, M. A. Controlling Conformations of Conjugated Polymers and Small Molecules: The Role of Nonbonding Interactions. *J. Am. Chem. Soc.* **2013**, *135* (28), 10475–10483.
- (36) Carpenter, J. H.; Ghasemi, M.; Gann, E.; Angunawela, I.; Stuard, S. J.; Rech, J. J.; Ritchie, E.; O'Connor, B. T.; Atkin, J.; You, W.; DeLongchamp, D. M.; Ade, H. Competition between Exceptionally Long-Range Alkyl Sidechain Ordering and Backbone Ordering in Semiconducting Polymers and Its Impact on Electronic and Optoelectronic Properties. *Adv. Funct. Mater.* **2019**, *29* (5), 1806977.
- (37) Jun, L.; Jiu-Xun, S.; Zhao, C. Improved Expression of Charge-Carrier Mobility in Disordered Semiconducting Polymers Considering Dependence on Temperature, Electric Field and Charge-Carrier Density. *Synth. Met.* **2009**, *159* (19), 1915–1921.
- (38) Yuan, X.-J.; Dong, X.-F.; Li, D.-M.; Liu, D.-S. Effects of Disordered Interchain Interactions on Polaron Dynamics in Semiconducting Polymers. *J. Chem. Phys.* **2011**, *134* (24), 244901.
- (39) Cottaar, J.; Bobbert, P. A. Calculating Charge-Carrier Mobilities in Disordered Semiconducting Polymers: Mean Field and Beyond. *Phys. Rev. B* **2006**, *74* (11), 115204.
- (40) Pasveer, W. F.; Cottaar, J.; Tanase, C.; Coehoorn, R.; Bobbert, P. A.; Blom, P. W. M.; de Leeuw, D. M.; Michels, M. A. J. Unified Description of Charge-Carrier Mobilities in Disordered Semiconducting Polymers. *Phys. Rev. Lett.* **2005**, *94* (20).
- (41) Perdew, J. P.; Yang, W.; Burke, K.; Yang, Z.; Gross, E. K. U.; Scheffler, M.; Scuseria, G. E.; Henderson, T. M.; Zhang, I. Y.; Ruzsinszky, A.; Peng, H.; Sun, J.; Trushin, E.; Görling, A. Understanding Band Gaps of Solids in Generalized Kohn-Sham Theory. *Proc. Natl. Acad. Sci. U. S. A.* **2017**, *114* (11), 2801–2806.
- (42) Katz, H. E. Stabilization and Specification in Polymer Field-Effect Transistor Semiconductors. *ACS Appl. Mater. Interfaces* **2022**, *14* (14), 15861–15.
- (43) Jun, L.; Jiu-Xun, S.; Zhao, C. Improved Expression of Charge-Carrier Mobility in Disordered Semiconducting Polymers Considering Dependence on Temperature, Electric Field and Charge-Carrier Density. *Synth. Met.* **2009**, *159* (19), 1915–1921.
- (44) Podzorov, V.; Menard, E.; Rogers, J. A.; Gershenson, M. E. Hall Effect in the Accumulation Layers on the Surface of Organic Semiconductors. *Phys. Rev. Lett.* **2005**, *95* (22), 226601.

- (45) Meijer, E. J.; De Leeuw, D. M.; Setayesh, S.; Van Veenendaal, E.; Huisman, B. H.; Blom, P. W. M.; Hummelen, J. C.; Scherf, U.; Klapwijk, T. M. Solution-Processed Ambipolar Organic Field-Effect Transistors and Inverters. *Nat. Mater.* **2003**, 2 (10), 678–682.
- (46) Reid, O. G.; Malik, J. A. N.; Latini, G.; Dayal, S.; Kopidakis, N.; Silva, C.; Stingelin, N.; Rumbles, G. The Influence of Solid-State Microstructure on the Origin and Yield of Long-Lived Photogenerated Charge in Neat Semiconducting Polymers. *J. Polym. Sci. Part B Polym. Phys.* **2012**, 50 (1), 27–37.
- (47) Kline, R. J.; McGehee, M. D. Morphology and Charge Transport in Conjugated Polymers. *J. Macromol. Sci. Part C* **2006**, 46 (1), 27–45.
- (48) Son, S. Y.; Lee, G.-Y.; Kim, S.; Park, W.-T.; Park, S. A.; Noh, Y.-Y.; Park, T. Control of Crystallite Orientation in Diketopyrrolopyrrole-Based Semiconducting Polymers via Tuning of Intermolecular Interactions. *ACS Appl. Mater. Interfaces* **2019**, 11 (11), 10751–10757.
- (49) Nicolet, C.; Deribew, D.; Renaud, C.; Fleury, G.; Brochon, C.; Cloutet, E.; Vignau, L.; Wantz, G.; Cramail, H.; Geoghegan, M.; Hadziioannou, G. Optimization of the Bulk Heterojunction Composition for Enhanced Photovoltaic Properties: Correlation between the Molecular Weight of the Semiconducting Polymer and Device Performance. *J. Phys. Chem. B* **2011**, 115 (44), 12717–12727.
- (50) Afraj, S. N.; He, G.-Y.; Lin, C.-Y.; Velusamy, A.; Huang, C.-Y.; Lin, P.-S.; Vegiraju, S.; Huang, P.-Y.; Ni, J.-S.; Yau, S.-L.; Tung, S.-H.; Minari, T.; Liu, C.-L.; Chen, M.-C. Solution-Processable Multifused Thiophene Small Molecules and Conjugated Polymer Semiconducting Blend for Organic Field Effect Transistor Application. *Adv. Mater. Technol.* **2021**, 6 (3), 2001028.
- (51) Dixon, A. G.; Visvanathan, R.; Clark, N. A.; Stingelin, N.; Kopidakis, N.; Shaheen, S. E. Molecular Weight Dependence of Carrier Mobility and Recombination Rate in Neat P3HT Films. *J. Polym. Sci. Part B Polym. Phys.* **2018**, 56 (1), 31–35.
- (52) Herrero, M.; Mendiola, J. A.; Cifuentes, A.; Ibáñez, E. Supercritical Fluid Extraction: Recent Advances and Applications. *J. Chromatogr. A* **2010**, 1217 (16), 2495–2511.
- (53) Brunner, G. Applications of Supercritical Fluids. *Annu. Rev. Chem. Biomol. Eng.* **2010**, 1 (1), 321–342.
- (54) Clifford, A. A.; Williams, J. R. Introduction to Supercritical Fluids and Their Applications BT - Supercritical Fluid Methods and Protocols; Williams, J. R., Clifford, A. A., Eds.; Humana Press: Totowa, NJ, 2000; pp 1–16.
- (55) Baker, L. E.; Pierce, A. C.; Luks, K. D. Gibbs Energy Analysis of Phase Equilibria. *Soc. Pet. Eng. AIME, SPE* **1981**, No. October, 471–488.

- (56) Choi, P. A Re-Examination of the Concept of Hildebrand Solubility Parameter for Polymers. *Macromol. Rapid Commun.* **2002**, 23 (8), 484–487.
- (57) Porter, J. D. The Solubility of Nonelectrolytes . 3rd Ed. Joel H. Hildebrand and Robert L. Scott. New York: Reinhold, 1950.
- (58) Hansen, C.M. (2007). Hansen Solubility Parameters: A User's Handbook, Second Edition (2nd ed.). CRC Press.
- (59) Venkatram, S.; Kim, C.; Chandrasekaran, A.; Ramprasad, R. Critical Assessment of the Hildebrand and Hansen Solubility Parameters for Polymers. *J. Chem. Inf. Model.* **2019**.
- (60) Zhao, Y.; Inbar, P.; Chokshi, H. P.; Malick, A. W.; Choi, D. S. Prediction of the Thermal Phase Diagram of Amorphous Solid Dispersions by Flory–Huggins Theory. *J. Pharm. Sci.* **2011**, 100 (8), 3196–3207.
- (61) Dudowicz, J.; Freed, K. F.; Douglas, J. F. Flory-Huggins Model of Equilibrium Polymerization and Phase Separation in the Stockmayer Fluid. *Phys. Rev. Lett.* **2004**, 92 (4), 4.
- (62) Yousefi, N.; Maala, J. J.; Louie, M.; Storback, J.; Kaake, L. G. Physical Supercritical Fluid Deposition: Patterning Solution Processable Materials on Curved and Flexible Surfaces. *ACS Appl. Mater. Interfaces* **2020**, 12 (15), 17949–17956.
- (62) Frigaard, I. A.; Nouar, C. On the Usage of Viscosity Regularisation Methods for Visco-Plastic Fluid Flow Computation. *J. Nonnewton. Fluid Mech.* **2005**, 127 (1), 1–26.
- (63) Ahlers, G.; Behringer, R. P. Evolution of Turbulence from the Rayleigh-Benard Instability. *Phys. Rev. Lett.* **1978**, 40 (11), 712–716.
- (64) Brown, J. Q.; Vishwanath, K.; Palmer, G. M.; Ramanujam, N. Advances in Quantitative UV–Visible Spectroscopy for Clinical and Pre-Clinical Application in Cancer. *Curr. Opin. Biotechnol.* **2009**, 20 (1), 119–131.
- (65) Grasse, E. K.; Torcasio, M. H.; Smith, A. W. Teaching UV–Vis Spectroscopy with a 3D-Printable Smartphone Spectrophotometer. *J. Chem. Educ.* **2016**, 93 (1), 146–151.
- (66) Root, S. E.; Alkhadra, M. A.; Rodriguez, D.; Printz, A. D.; Lipomi, D. J. Measuring the Glass Transition Temperature of Conjugated Polymer Films with Ultraviolet–Visible Spectroscopy. *Chem. Mater.* **2017**, 29 (7), 2646–2654.
- (67) Antonov, L.; Nedeltcheva, D. Resolution of Overlapping UV-Vis Absorption Bands and Quantitative Analysis. *Chem. Soc. Rev.* **2000**, 29 (3), 217–227.

- (68) Coon, J. B.; DeWames, R. E.; Loyd, C. M. The Franck-Condon Principle and the Structures of Excited Electronic States of Molecules. *J. Mol. Spectrosc.* **1962**, *8* (1), 285–299.
- (69) Swinehart, D. F. The Beer-Lambert Law. *J. Chem. Educ.* **1962**, *39* (7), 333–335.
- (70) Zhu, S.; Hou, F.; Huang, W.; Yao, X.; Shi, B.; Ren, Q.; Chen, J.; Yan, L.; An, S.; Zhou, Z.; Ren, H.; Wei, C.; Huang, Q.; Li, Y.; Hou, G.; Chen, X.; Ding, Y.; Wang, G.; Li, B.; Zhao, Y.; Zhang, X. Solvent Engineering to Balance Light Absorbance and Transmittance in Perovskite for Tandem Solar Cells. *Sol. RRL* **2018**, *2* (11), 1800176.
- (71) Chen, X.-X.; Li, J.-T.; Fang, Y.-H.; Deng, X.-Y.; Wang, X.-Q.; Liu, G.; Wang, Y.; Gu, X.; Jiang, S.-D.; Lei, T. High-Mobility Semiconducting Polymers with Different Spin Ground States. *Nat. Commun.* **2022**, *13* (1), 2258.
- (72) Pitsalidis, C.; Pappa, A. M.; Hunter, S.; Laskarakis, A.; Kaimakamis, T.; Payne, M. M.; Anthony, J. E.; Anthopoulos, T. D.; Logothetidis, S. High Mobility Transistors Based on Electro spray-Printed Small-Molecule/Polymer Semiconducting Blends. *J. Mater. Chem. C* **2016**, *4* (16), 3499–3507.
- (73) Pasveer, W. F.; Cottaar, J.; Tanase, C.; Coehoorn, R.; Bobbert, P. A.; Blom, P. W. M.; de Leeuw, D. M.; Michels, M. A. J. Unified Description of Charge-Carrier Mobilities in Disordered Semiconducting Polymers. *Phys. Rev. Lett.* **2005**, *94* (20).
- (75) Zaumseil, J.; Sirringhaus, H. Electron and Ambipolar Transport in Organic Field-Effect Transistors. *Chem. Rev.* **2007**, *107* (4), 1296–1323.
- (76) Simon, C. M.; Kaminsky, W. Chemical Recycling of Polytetrafluoroethylene by Pyrolysis. *Polym. Degrad. Stab.* **1998**, *62* (1), 1–7.
- (77) Lior, N. Chapter 1.2 Measurement of Small Temperature and Pressure Differences. *Desalination* **1986**, *59*, 19–60.
- (78) Savagatrup, S.; Printz, A. D.; O'Connor, T. F.; Zaretski, A. V; Lipomi, D. J. Molecularly Stretchable Electronics. *Chem. Mater.* **2014**, *26* (10), 3028–3041.
- (79) Fang, F. Z.; Zhang, X. D.; Gao, W.; Guo, Y. B.; Byrne, G.; Hansen, H. N. Nanomanufacturing—Perspective and Applications. *CIRP Ann.* **2017**, *66* (2), 683–705
- (80) Cooper, K. Scalable Nanomanufacturing—A Review. *Micromachines* **2017**, *8* (1).
- (81) Liddle, J. A.; Gallatin, G. M. Nanomanufacturing: A Perspective. *ACS Nano* **2016**, *10* (3), 2995–3014.

- (82) Biswas, A.; Bayer, I. S.; Biris, A. S.; Wang, T.; Dervishi, E.; Faupel, F. Advances in Top-down and Bottom-up Surface Nanofabrication: Techniques, Applications & Future Prospects. *Adv. Colloid Interface Sci.* **2012**, *170* (1–2), 2–27.
- (83) Yousefi, N.; Saeedi Saghez, B.; Pettipas, R. D.; Kelly, T. L.; Kaake, L. G. The Role of Solvent Additive in Polymer Crystallinity during Physical Supercritical Fluid Deposition. *New J. Chem.* **2021**, *45* (26), 11786–11796.
- (84) Yousefi, N.; Saeedi Saghez, B.; Pettipas, R. D.; Kelly, T. L.; Kaake, L. G. Physical Supercritical Fluid Deposition of Polymer Films: Controlling the Crystallinity with Pressure. *Mater. Chem. Front.* **2021**, *5* (3), 1428–1437.
- (85) Yousefi, N.; Pettipas, R. D.; Kelly, T. L.; Kaake, L. G. Self-Assembly of PBTTT–C14 Thin Films in Supercritical Fluids. *Mater. Adv.* **2022**, *3* (5), 2515–2523.
- (86) Barim, S. B.; Uzunlar, E.; Bozbag, S. E.; Erkey, C. Review—Supercritical Deposition: A Powerful Technique for Synthesis of Functional Materials for Electrochemical Energy Conversion and Storage. *J. Electrochem. Soc.* **2020**, *167* (5), 054510.
- (87) Yang, J.; Hasell, T.; Smith, D. C.; Howdle, S. M. Deposition in Supercritical Fluids: From Silver to Semiconductors. *J. Mater. Chem.* **2009**, *19* (45), 8560–8570.
- (88) Blackburn, J. M.; Long, D. P.; Cabanas, A.; Watkins, J. J. Deposition of Conformal Copper and Nickel Films from Supercritical Carbon Dioxide. *Science* **2001**, *294* (5540), 141–145.
- (89) Cabañas, A.; Long, D. P.; Watkins, J. J. Deposition of Gold Films and Nanostructures from Supercritical Carbon Dioxide. *Chem. Mater.* **2004**, *16* (10), 2028–2033.
- (90) Wei, Q.; You, E.; Hendricks, N. R.; Briseno, A. L.; Watkins, J. J. Flexible Low-Voltage Polymer Thin-Film Transistors Using Supercritical CO₂-Deposited ZrO₂ Dielectrics. *ACS Appl. Mater. Interfaces* **2012**, *4* (5), 2322–2324.
- (91) You, E.; Guzmán-Blas, R.; Nicolau, E.; Aulice Scibioh, M.; Karanikas, C. F.; Watkins, J. J.; Cabrera, C. R. Co-Deposition of Pt and Ceria Anode Catalyst in Supercritical Carbon Dioxide for Direct Methanol Fuel Cell Applications. *Electrochim. Acta* **2012**, *75*, 191–200.
- (92) Li, L.; Counts, K. E.; Kurosawa, S.; Teja, A. S.; Collard, D. M. Tuning the Electronic Structure and Solubility of Conjugated Polymers with Perfluoroalkyl Substituents: Poly(3-Perfluorooctylthiophene), the First Supercritical CO₂-Soluble Conjugated Polymer. *Adv. Mater.* **2004**, *16* (2), 180–183.
- (93) Anderson, P. E.; Badlani, R. N.; Mayer, J.; Mabrouk, P. A. Electrochemical Synthesis and Characterization of Conducting Polymers in Supercritical Carbon Dioxide. *J. Am. Chem. Soc.* **2002**, *124* (35), 10284–10285.

- (94) Castro, A.; Morère, J.; Cabañas, A.; Ferreira, L. P.; Godinho, M.; Ferreira, P.; Vilarinho, P. M. Designing Nanocomposites Using Supercritical CO₂ to Insert Ni Nanoparticles into the Pores of Nanopatterned BaTiO₃ Thin Films. *J. Mater. Chem. C* **2017**, *5* (5), 1083–1089.
- (95) Forrest, S. R. The Path to Ubiquitous and Low-Cost Organic Electronic Appliances on Plastic. *Nature* **2004**, *428* (6986), 911–918.
- (96) Himmelberger, S.; Salleo, A. Engineering Semiconducting Polymers for Efficient Charge Transport. *MRS Commun.* **2015**, *5* (3), 383–395.
- (97) Taylor, P. G.; Lee, J.-K.; Zakhidov, A. A.; Chatzichristidi, M.; Fong, H. H.; DeFranco, J. A.; Malliaras, G. G.; Ober, C. K. Orthogonal Patterning of PEDOT:PSS for Organic Electronics Using Hydrofluoroether Solvents. *Adv. Mater.* **2009**, *21* (22), 2314–2317.
- (98) Yang, C.-Y.; Tu, D.; Ruoko, T.-P.; Gerasimov, J. Y.; Wu, H.-Y.; Harikesh, P. C.; Massetti, M.; Stoeckel, M.-A.; Kroon, R.; Müller, C.; Berggren, M.; Fabiano, S. Low-Power/High-Gain Flexible Complementary Circuits Based on Printed Organic Electrochemical Transistors. *Adv. Electron. Mater.* **2022**, *8* (3), 2100907.
- (99) Jensen, J.; Hösel, M.; Dyer, A. L.; Krebs, F. C. Development and Manufacture of Polymer-Based Electrochromic Devices. *Adv. Funct. Mater.* **2015**, *25* (14), 2073–2090
- (100) Baeg, K.-J.; Caironi, M.; Noh, Y.-Y. Toward Printed Integrated Circuits Based on Unipolar or Ambipolar Polymer Semiconductors. *Adv. Mater.* **2013**, *25* (31), 4210–4244.
- (101) Cho, J. H.; Lee, J.; Xia, Y.; Kim, B.; He, Y.; Renn, M. J.; Lodge, T. P.; Frisbie, C. D. Printable Ion-Gel Gate Dielectrics for Low-Voltage Polymer Thin-Film Transistors on Plastic. *Nat. Mater.* **2008**, *7* (11), 900–906.
- (102) Tait, J. G.; Witkowska, E.; Hirade, M.; Ke, T.-H.; Malinowski, P. E.; Steudel, S.; Adachi, C.; Heremans, P. Uniform Aerosol Jet Printed Polymer Lines with 30µm Width for 140ppi Resolution RGB Organic Light Emitting Diodes. *Org. Electron.* **2015**, *22*, 40–43.
- (103) Simeoni, G. G.; Bryk, T.; Gorelli, F. A.; Krisch, M.; Ruocco, G.; Santoro, M.; Scopigno, T. The Widom Line as the Crossover between Liquid-like and Gas-like Behaviour in Supercritical Fluids. *Nat. Phys.* **2010**, *6* (7), 503–507.
- (104) Tony Clifford - Fundamentals of Supercritical Fluids-Oxford University Press, USA (1999).
- (105) Xudong An; Arora, M.; Wei Huang; Brantley, W. C.; Greathouse, J. L. 3D Numerical Analysis of Two-Phase Immersion Cooling for Electronic Components. *2018 17th IEEE Intersoc. Conf. Therm. Thermomechanical Phenom. Electron. Syst.* **2018**, 609–614.

- (106) Hulse, R. J.; Basu, R. S.; Singh, R. R.; Thomas, R. H. P. Physical Properties of HCFO-1233zd(E). *J. Chem. Eng. Data* **2012**, *57* (12), 3581–3586.
- (107) Hiemenz, P.C., & Lodge, T.P. (2007). *Polymer Chemistry* (2nd ed.) CRC Press.
- (108) Kirby, C. F.; McHugh, M. A. Phase Behavior of Polymers in Supercritical Fluid Solvents. *Chem. Rev.* **1999**, *99* (2), 565–602.
- (109) Patterson, D. Polymer Compatibility with and without a Solvent. *Polym. Eng. & Sci.* **1982**, *22* (2), 64–73.
- (110) Eckert, C. A.; Knutson, B. L.; Debenedetti, P. G. Supercritical Fluids as Solvents for Chemical and Materials Processing. *Nature* **1996**, *383* (6598), 313–318.
- (111) Abo-Zahhad, E. M.; Ookawara, S.; Radwan, A.; Memon, S.; Yang, Y.; El-Kady, M. F.; El-Shazly, A. H. Flow Boiling in a Four-Compartment Heat Sink for High-Heat Flux Cooling: A Parametric Study. *Energy Convers. Manag.* **2021**, *230*, 113778.
- (112) Spano, F. C. The Spectral Signatures of Frenkel Polarons in H- and J-Aggregates. *Acc. Chem. Res.* **2010**, *43* (3), 429–439
- (113) Hestand, N. J.; Spano, F. C. Expanded Theory of H- and J-Molecular Aggregates: The Effects of Vibronic Coupling and Intermolecular Charge Transfer. *Chem. Rev.* **2018**, *118* (15), 7069–7163.
- (114) Scharsich, C.; Lohwasser, R. H.; Sommer, M.; Asawapirom, U.; Scherf, U.; Thelakkat, M.; Neher, D.; Köhler, A. Control of Aggregate Formation in Poly(3-Hexylthiophene) by Solvent, Molecular Weight, and Synthetic Method. *J. Polym. Sci. Part B Polym. Phys.* **2012**, *50* (6), 442–453.
- (115) Patten, K. O.; Wuebbles, D. J. Atmospheric Lifetimes and Ozone Depletion Potentials of Trans-1-Chloro-3,3,3-Trifluoropropylene and Trans-1,2-Dichloroethylene in a Three-Dimensional Model. *Atmos. Chem. Phys.* **2010**, *10* (22), 10867–10874.
- (116) Kim, T. G.; Jeong, E. H.; Lim, S. C.; Kim, S. H.; Kim, G. H.; Kim, S. H.; Jeon, H. Y.; Youk, J. H. PMMA-Based Patternable Gate Insulators for Organic Thin-Film Transistors. *Synth. Met.* **2009**, *159* (7–8), 749–753.